
TREATMENT LEARNING CAUSAL TRANSFORMER FOR NOISY IMAGE CLASSIFICATION

A PREPRINT

Chao-Han Huck Yang*
Georgia Institute of Technology
huckiyang@gatech.edu

I-Te Danny Hung*
Columbia University
ih2320@columbia.edu

Yi-Chieh Liu*
Georgia Institute of Technology
yliu3233@gatech.edu

Pin-Yu Chen
IBM Research
pin-yu.chen@ibm.com

October 31, 2023

ABSTRACT

Current top-notch deep learning (DL) based vision models are primarily based on exploring and exploiting the inherent correlations between training data samples and their associated labels. However, a known practical challenge is their degraded performance against “noisy” data, induced by different circumstances such as spurious correlations, irrelevant contexts, domain shift, and adversarial attacks. In this work, we incorporate this binary information of “existence of noise” as treatment into image classification tasks to improve prediction accuracy by jointly estimating their treatment effects. Motivated from causal variational inference, we propose a transformer-based architecture, Treatment Learning Causal Transformer (TLT), that uses a latent generative model to estimate robust feature representations from current observational input for noise image classification. Depending on the estimated noise level (modeled as a binary treatment factor), TLT assigns the corresponding inference network trained by the designed causal loss for prediction. We also create new noisy image datasets incorporating a wide range of noise factors (e.g., object masking, style transfer, and adversarial perturbation) for performance benchmarking. The superior performance of TLT in noisy image classification is further validated by several refutation evaluation metrics. As a by-product, TLT also improves visual salience methods for perceiving noisy images.

1 Introduction

Although deep neural networks (DNNs) have surpassed human-level “accuracy” in many image recognition tasks [Ronneberger et al., 2015, He et al., 2016, Huang et al., 2017], current DNNs still implicitly rely on the *assumption* [Pearl, 2019] on the existence of a strong correlation between training and testing data. Moreover, increasing evidence and concerns [Alcorn et al., 2019] show that using the correlation association for prediction can be problematic against *noisy* images [Xiao et al., 2015], such as pose-shifting of identical objects [Alcorn et al., 2019] or imperceptible perturbation [Goodfellow et al., 2015]. In practice, real-world image classification often involves rich, noisy, and even chaotic contexts, intensifying the demand for generalization in the wild. Putting in a unified descriptive framework,

To address machine perception against noisy images, we are inspired by how human performs visual recognition. Human’s learning processes are often mixed with logic inference (e.g., a symbolic definition from books) and representation learning (e.g., an experience of viewing a visual pattern). One prominent difference between current DNNs and human recognition systems is the capability in causal inference. Mathematically, causal learning [Pearl, 1995a, Peters et al., 2014] is a statistical inference model that infers beliefs or probabilities under uncertain conditions, which aims to identify latent variables (called “confounders”) that influence both intervention and outcome. The unobserved confounders may be abstract in a cognitive-level (e.g., concepts) but could be observed via their noisy view in the real-world (e.g., objects). For instance, as shown in Fig. 1 (a), confounder learning aims to model a prediction process



Figure 1: (a) An example of deployed causal graphical model (CGM), where Z denotes unobservable confounder variable (e.g., the concept of “cat”), X denotes a noisy observation of confounder (e.g., an image can still be recognized as a cat), y denotes outcome (e.g., a label), and t denotes the information of a binary treatment (e.g., the existence of extra semantic patterns or additive noise; thus, it is equal to 0 or 1), which is **observable** during **training** and **unobservable** during **testing** time. (b) Images with “cat” labels, where (i) and (ii) share the same context of “indoor”; (iii) shows a noisy setup of (ii) undergoing additive Gaussian perturbation; (iv) shows another setup of introducing extra noisy semantic patterns (e.g., “waterside”) in NICO [He et al., 2020] noisy images dataset.

by finding a representation (e.g., “cat”) and avoiding relying on irrelevant patterns (e.g., “waterside”). Intuitively, with causal modeling and confounder inference, correct prediction can be made on noisy inputs, where the generative estimation process, such as causal effect variational autoencoder (CEVAE) [Louizos et al., 2017], affects multiple covariates for predicting data profiles. In this work, we aim to incorporate the effects of causal confounder learning to image classification, as motivated by cognitive psychology for causal learning. Specifically, we use the attention mechanism for noise-resilience inference from patterns. We design a novel sequence-to-sequence learning model, **Treatment Learning Causal Transformer (TLT)**, which leverages upon the conditional query-based attention and the inference power from a variational causal inference model.

Our TLT tackles noisy image classification by jointly learning to a generative model of Z and estimating the effects from the treatment information (t), as illustrated in Fig. 1 (a). This model consists of unobservable confounder variables Z corresponding to the ground-truth but inaccessible information (e.g., the ontological concept [Trampusch and Palier, 2016] of a label), input data X from a noisy view of Z (e.g., images), a treatment [Pearl et al., 2016] information t given X and Z (e.g., secondary information as visual patterns and additive noise without directly affecting our understanding the concept of “cat”), and a classification label y from the unobservable confounder. Built upon this causal graphical model, our contributions are:

- A transformer architecture (TLT) for noisy image classification are presented, which is based on a treatment estimation architecture and a causal variational generative model with competitive classification performance against noisy image.
- We further curated a new noisy images datasets, Causal Pairs (CPS), to study generalization under different artificial noise settings for general and medical images.
- We use formal statistical refutations tests to validate the causal effect of TLT, and show that TLT can improve visual saliency methods on noisy images.

2 Related Work

Noisy Image Classification. Prior works on noisy images classification have highlighted the importance of using generative models [Oquab et al., 2014] to ameliorate the negative learning effects from noisy data. Xiao *et al.* [Xiao et al., 2015] leverage a conditional generative model [Sohn et al., 2015] to capture the relations among images and noise types from online shopping systems. Direct learning from noisy data is another approach by using statistical sampling [Han et al., 2019, Li et al., 2017] and active learning [Gal et al., 2017] for performance enhancement. Meanwhile, new noisy images dataset and evaluation metrics [He et al., 2020] on context independence have been proposed, such as Strike simulator [Alcorn et al., 2019] for synthesizing pose-shifting images and NICO [He et al., 2020, Zhang et al., 2021, Liu et al., 2021] as the open-access noisy image dataset. NICO further aims to highlight the importance of incorporating a statistical inference (e.g., causal model) for improved image classification with large-scale noisy context-patterns (e.g., an image shows “cat in waterside” but given a single label of “cat”). However, different from context-wise noise in NICO, modeling sizeable artificial noise in images is crucial yet remains unexplored. In this work, we create a new image dataset containing various artificial noise and use the NICO [He et al., 2020] with a generative causal model for performance benchmarking.

Causal Learning for Computer Vision. Many efforts [Pickup et al., 2014, Fire and Zhu, 2016, Lebeda et al., 2015, Fire and Zhu, 2013] have leveraged upon causal learning to better understand and interpret toward vision recognition tasks. Lopez-Paz *et al.* [Lopez-Paz et al., 2017] propose utilizing DNNs to discover the causation between image class labels

for addressing the importance of this direct causal relationship affecting model performance and context grounding. Incorporating causal analysis and regularization showed improved performance in generative adversarial models such as Causal-GANs [Kocaoglu et al., 2017, Bahadori et al., 2017]. However, infusing causal modeling and inference to DNN-based image recognition systems is still an open challenge. For instance, in previous works [Lopez-Paz et al., 2017, Yang et al., 2019], researchers focus on modeling a direct causal model (DCM) [Pearl et al., 2016] for visual learning. The DCMs treat a visual pattern (e.g., texture) as a cause visual representation (e.g., patterns of the “cat”) and barely incorporate additional label information (e.g., context) or apply noise as a **treatment** in causal analysis. In recent works, causal modeling also show promising results in a large-scale computer vision task, such scene graph [Tang et al., 2020] generation, visual and language learning [Qi et al., 2020, Agarwal et al., 2020, Abbasnejad et al., 2020], and semantic segmentation [Zhang et al., 2020]. The work of Chalupka et al. [Chalupka et al., 2014] is closer to our work by deploying interventional experiments to target causal relationships in the labeling process. However, modeling the aforementioned treatment effects and designing efficient learning models are still not fully explored [Pearl, 2019].

Causal Inference by Autoencoder. Recently, classical causal inference tasks, such as regression modeling [Bühlmann et al., 2014], risk estimation [Pearl, 2019], and causal discovery [Monti et al., 2020], have been incorporated with deep generative models [Rezende et al., 2014] and attained state-of-the-art performance [Shalit et al., 2017, Louizos et al., 2017]. These generative models often use an encoder-decoder architecture to improve both logic inference and features extracted from a large-scale dataset with noisy observations. TARNet [Shalit et al., 2017] is one foundational DNN model incorporating causal inference loss from a causal graphical model (CGM) and feature reconstruction loss jointly for linear regression, showing better results compared with variational inference models [Kingma and Welling, 2013]. Inspired by the CGM of TARNet [Shalit et al., 2017], causal-effect variational autoencoder (CEVAE) was proposed in [Louizos et al., 2017, Yang et al., 2021] for regression tasks, which draws a connection between causal inference with proxy variables and latent space learning for approximating the hidden and unobservable confounder by the potential outcome model from Rubin’s causal inference framework [Imbens and Rubin, 2010, Rubin, 1974]. Our proposed causal model in TLT shares a similar CGM with CEVAE but has a different training objective, probabilistic encoding, and specific design for visual recognition, such as the use of attention mechanism.

3 TLT: Treatment Learning Causal Transformer

3.1 Modeling under Causal Hierarchy Theorem

To model a general image classification problem with causal inference, we introduce Pearl’s *causal hierarchy Theorem* [Bareinboim et al., 2020, Shpitser and Pearl, 2008, Pearl, 2009] as shown in Tab. 1, with a non-causal classification model and a causal inference model. Non-causal model is in level (II) of causal hierarchy, which associates the *outcome* (prediction) to the input directly by $P(y|x)$ from supervised model such as ResNet [He et al., 2016]. Non-causal model could be unsupervised by using approximate inference such as variational encoder-decoder [Bahuleyan et al., 2018] with two parameterized networks, Θ and Φ . The association-level (non-causal) setup in the causal hierarchy can solve visual learning tasks at level (II), such as non-noisy image classification.

Table 1: *Causal hierarchy* [Pearl, 2009]: questions at level i can only be answered if information from the same or higher level is available.

Level	Activity	PGM	Example
(I) Association	Observing	$P(y x)$	ResNet [He et al., 2016]
(II) Intervention	Intervening	$P(y do(x), z)$	TLT (ours)

For noisy image classification, we argue that the problem setup is elevated to level (III) of the causal hierarchy, requiring the capability of confounder learning and the *do-calculus* [Pearl, 2019] (refer to causal inference foundations **supplement A**). We first make a formal definition on a pair of i^{th} query (x_i, y_i) including a noisy image input (x_i) and its associated label (y_i) . Suppose for every noisy image, there exists a clean but inaccessible image (\tilde{x}_i) and treatment information (t_i) , where the intervened observation is modeled as $P(x_i) = P(do(\tilde{x}_i)) \equiv P(\tilde{x}_i|t_i)$, and t_i encodes full information of the intervention through the do-operator notation $do(\cdot)$. The corresponding confounder z_i follows $P(z_i) = P(\tilde{x}_i, t_i, \tilde{z}_i)$, where \tilde{z}_i is the unobservable part (e.g., undiscovered species of “cat” but belong to its ontological definition) of the confounder. To make a prediction (y_i) of a noisy input of (x_i) , we could have the intervened view of the question by:

$$P(y_i|x_i) = P(y_i|do(\tilde{x}_i), z_i) = P(y_i|\tilde{x}_i, t_i, z_i) \quad (1)$$

with do-operator in level (III) of the causal hierarchy. Based on the causal hierarchy, we could use the model with the proxy variables (z_i, t_i) in the higher level (III) to answer the question in equal or lower level. Next, we introduce our training objective using an encoder-decoder architecture to reparameterize the aforementioned proxy variables for causal learning.

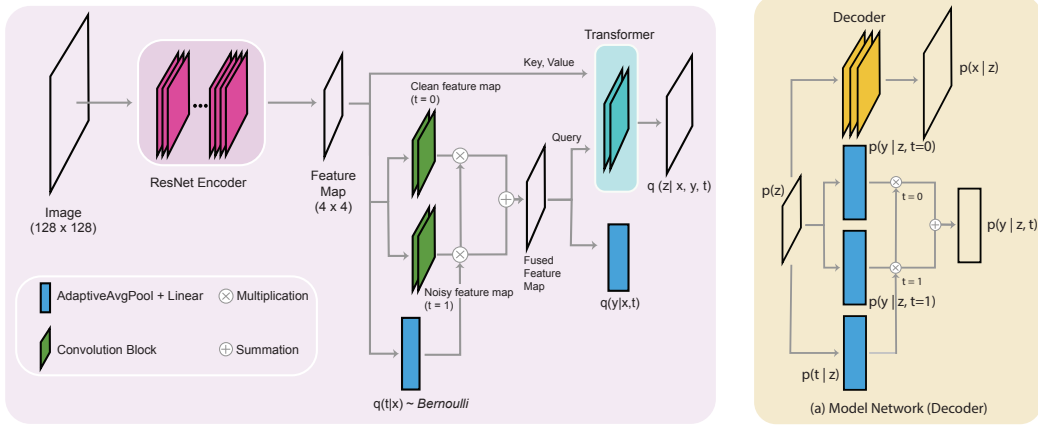


Figure 2: The encoder (inference network) structure of our proposed causal transformer. We leverage bilinear fusion (BF) for $q(z|x, y, t)$ instead of concatenation [Louizos et al., 2017], and decoding conditional queries $H_z \sim q(y|x, t)$ and encoding features $H_x \sim p(x)$ as keys and values to conduct attention. Decoder model is shown as Fig. 2 (a) with potential outcome modeling [Imbens and Rubin, 2010, Rubin, 1974] from $p(z)$.

3.2 Training Objective of TLT

We build our TLT model based on the foundational framework of conditional variational encoder-decoder (CVED) [Bahuleyan et al., 2018, Kingma and Welling, 2013], which learns a variational latent representation z_i from data x_i and conditional information (e.g., label y_i) for reconstruction or recognition. To effectively learn visual causal pattern recognition, our TLT model uses variational inference to approximate the complex non-linear relationships involving: the pair probability ($p(x_i, z_i)$), the treatment likelihood $P(t_i)$, the model outcome $p(y_i)$, and the joint distribution $p(z_i, x_i, t_i, y_i)$. Specifically, we propose to characterize the causal graphical model in Fig. 1 (a) as a latent variable model parameterized by a DNN encoder-decoder as shown in Fig. 6 (in Appendix A). Note that TLT uses an advanced decoding method $p(a_i) = F_T(H_x, H_z \sim P(x_i))$ for approximating $p(z_i)$ from $p(x_i)$ based on the attention (F_T) from transformer [Vaswani et al., 2017], which will be detailed in Sec. 3.3.

First, we assume the observations factorize conditioned on the latent variables and use an *general* inference network (encoder) which follows a factorization of the true posterior. For the model network (decoder), instead of conditioning on observations, we approximate the latent variables z . For vision tasks, x_i corresponds to a noisy input image indexed by i , $t_i \in \{0, 1\}$ corresponds to the treatment assignment, y_i corresponds to the outcome and z_i corresponds to the latent hidden confounder. Note that general formation of an approximation outcome (δ) is modeling by $\delta_i = t_i \cdot y_i + (1 - t_i) \cdot y_i$ as potential outcome model [Imbens and Rubin, 2010, Holland, 1986] with its foundation over the causal inference. Next, each of the corresponding factors is described as:

$$p(z_i) = \prod_{z \in z_i} \mathcal{N}(z|0, 1); \quad p(x_i|z_i) = \prod_{x \in x_i} p(x|z_i); \quad p(t_i|z_i) = \text{Bern}(\sigma(f_1(z_i)));$$

$$p(y_i|z_i, t_i) = \sigma(t_i f_2(z_i) + (1 - t_i) f_3(z_i))$$

with $\mathcal{N}(\mu, \sigma^2)$ denoting a Gaussian distribution with mean μ and variance σ^2 , $p(x|z_i)$ being an appropriate probability distribution, $\sigma(\cdot)$ being a logistic function, and $\text{Bern}(\cdot)$ denotes the probability of success of a Bernoulli random variable. Each of the $f_k(\cdot)$ function is an Adaptive Average Pooling plus Linear layer parameterized by its own parameters θ_k for $k = \{1, 2, 3\}$. Here y_i is tailored for categorical classification problems, but our formulation can be naturally extended to different tasks. For example, one can simply remove the final $\sigma(\cdot)$ layer of $p(y_i|z_i, t_i)$ for regression tasks.

Our TLT inference network (encoder), as illustrated in Fig. 2, aims to learn meaningful causal representations in the latent space. As we can see from Fig. 1 (a), the true posterior over $z \in \mathbf{Z}$ depends on $x \in \mathbf{X}$, t , and y . We are required to know the treatment assignment t along with its outcome y prior to inferring the distribution over z . Therefore, unlike variational encoders, which simply passes the feature map directly to latent space (the top path in our encoder), the feature map extracted from a residual block is provided to the other switching (the lower and middle paths in our encoder), which provides posterior estimates of treatment t_i and outcome y_i . The switching mechanism (binary selection based on the treatment information of $t_i = 0$ or 1) and its alternative loss training have been widely used in TARNet [Shalit et al., 2017] and CEVAE [Louizos et al., 2017] with theoretical and empirical justification. We employ

the distribution by the switching mechanism:

$$q(t_i|x_i) = \text{Bern}(\sigma(g_1(x_i))); \quad (2)$$

$$q(y_i|x_i, t_i) = \sigma(t_i g_2(x_i) + (1 - t_i) g_3(x_i)), \quad (3)$$

with each g_k being a neural network approximating $q(t_i|x_i)$ or $q(y_i|x_i, t_i)$. They introduce auxiliary distributions that help us predict t_i and y_i for new samples. To optimize these two distributions, we add an auxiliary objective to our overall model training objective over N data samples:

$$\mathcal{L}_{aux} = \sum_{i=1}^N (\log q(t_i = t_i^*|x_i^*) + \log q(y_i = y_i^*|x_i^*, t_i^*)), \quad (4)$$

where x_i^* , t_i^* and y_i^* are the observed values in training set. Since the true posterior over z depends on x , t and y , finally we employ the posterior approximation below:

$$q(z_i|x_i, y_i, t_i) = \prod \mathcal{N}(\boldsymbol{\mu}_i, \boldsymbol{\sigma}_i^2) \quad (5)$$

$$\boldsymbol{\mu}_i = t_i \boldsymbol{\mu}_{t=1,i} + (1 - t_i) \boldsymbol{\mu}_{t=0,i}, \quad \boldsymbol{\sigma}_i^2 = t_i \boldsymbol{\sigma}_{t=1,i}^2 + (1 - t_i) \boldsymbol{\sigma}_{t=0,i}^2$$

$$\boldsymbol{\mu}_{t=0,i} = g_4 \circ g_0(x_i, y_i), \quad \boldsymbol{\sigma}_{t=0,i}^2 = \sigma(g_5 \circ g_0(x_i, y_i))$$

$$\boldsymbol{\mu}_{t=1,i} = g_6 \circ g_0(x_i, y_i), \quad \boldsymbol{\sigma}_{t=1,i}^2 = \sigma(g_7 \circ g_0(x_i, y_i))$$

where g_k again denotes neural network approximation, and $g_0(x_i, y_i)$ is a shared, bilinear-fused representation of x , t and y . More specifically, we multiply the feature map with approximated posterior $q(y_i|x_i, t_i)$ without logistic function σ to get $g_0(x_i, y_i)$. Finally, we can have the overall training objective for the inference and model networks. The variational lower bound of TLT to be optimized is given by:

$$\mathcal{L}_{TLT} = \mathcal{L}_{aux} + \sum_{i=1}^N \mathbb{E}_{q(z_i|x_i, t_i, y_i)} [\log p(x_i, t_i|z_i) + \log p(y_i|t_i, z_i) + \log p(z_i) - \log q(z_i|x_i, t_i, y_i)]. \quad (6)$$

As shown in Fig. 6 (in Appendix A), we could model $q(t|x) \doteq p(t)$ to access the treatment information directly for training to guide one corresponding sub-network in Fig. 2; for testing, $q(t|x)$ could be inferred by a given input x without knowing treatment information from an unsupervised perspective.

3.3 Attention mechanism of TLT

Attention mechanism is one of the human learning components to capture global dependencies for discovering logical and causal relationships [Nauta et al., 2019] from visual patterns in the cognitive psychology community [Chen et al., 2015]. Transformer [Vaswani et al., 2017] based attention mechanism has, recently, shown its connection from the **sequential** energy update rule to Hopfield networks [Ramsauer et al., 2020], which stands for a major framework to model human memory. With the intuition on leveraging human-inspired attention upon inference from noisy images, we incorporate a new type of Transformer module for the proposed causal modeling, which explicitly model all pairwise interactions between elements in a sequence. The idea is to learn the causal signal [Lopez-Paz et al., 2017] via self-attention setup, where we set the interference signal (H_z) for learning query and image features (H_x) for learning key and value. As shown in Fig 2, we use a feature map with a ResNet₃₄ [He et al., 2016] encoder extracting from input image $p(x_i)$ feeding into keys (K) and value (V) with queries $q(y_i)$ from Eq. (3):

$$Q = \text{unroll}(F_Q(H_z \sim q(y_i|x_i, t_i))); \quad K = \text{unroll}(F_K(H_x \sim p(x_i))) \quad (7)$$

$$V = \text{unroll}(F_V(H_x \sim p(x_i))); \quad a_i = \text{softmax}\left(\frac{QK^T}{\sqrt{d_k}}\right)V \quad (8)$$

where F_Q , F_K , F_V are convolutional neural networks and d_k is dimension of keys. Finally, we model $q(z_i)$ by using $q(t_i|x_i)$ and $p(a_i|x_i)$ with the causal two model extended from Eq. (5) for approximating posterior distribution $p(z_i)$:

$$p(z_i) \leftarrow q(z_i|x_i, a_i, y_i, t_i) = \prod_{z_i} \mathcal{N}(\boldsymbol{\mu}_i, \boldsymbol{\sigma}_i^2). \quad (9)$$

We also have conducted ablation studies on architecture selection and required parameters with respect to supervised learning [He et al., 2016], attention networks [Vaswani et al., 2017], and causal model [Shalit et al., 2017] in **supplement B** to validate our model design of TLT. To sum up, the proposed causal architecture attains the best performance with the same amount of parameters.

Table 2: Applying causal modeling on noisy images classification. **Case 1:** perfect labeled visual pattern (H_{lab}) with secondary patterns (H_{iid}); **Case 2:** original labeled images (H_{ori}) under an additive perturbation (F_{per}).

Treatment	\tilde{x}	$do(\tilde{x})$	$t=1$ or 0
1. Context	H_{lab}	$H_{lab} + H_{iid}$	Additional patterns (e.g., “waterside”) (1) or not (0)
2. Perturbation	H_{ori}	$F_{per}(H_{ori})$	Artificial noise (e.g., Gaussian) (1) or not (0)

4 Evaluating Causal Effects on Noisy Images

In this section, we introduce noisy image datasets and conduct statistical refutation tests on TLT to evaluate its causal effect based on the CGM in Fig. 1 (a). That is, we provide an affirmative answer to whether there **exist causal effects** in the studied noisy image classification tasks.

4.1 Estimate Causal Effects

Estimation of **expected causal effects** is one general approach [Pearl, 2019, 2009, Louizos et al., 2017] to evaluate whether a CGM (from a logic hypothesis) is valid on the selected test dataset. The underlying graphical model will undergo a series of randomization tests of graphical connection and sub-set sampling to measure its estimation errors on estimating causal effects. In general, a causal model is reliable with the CGM when exhibiting a lower absolute error on the causal effects. In this work, we use average treatment effects (ATE), as used in prior arts [Louizos et al., 2017], for comprehensive analysis.

Average Treatment Effects (ATEs). In the binary treatment setting [Pearl, 1995a], for the i -th individual and its associated model outcome y_i considering the treatment effect, the ATE is calculated by:

$$y_i = y_{t_i=0,i}(1 - t_i) + y_{t_i=1,i}(t_i), \quad (10)$$

$$ATE = |\mathbb{E}[y_i = y_i^* | t_i^* = 1] - \mathbb{E}[y_i = y_i^* | t_i^* = 0]|, \quad (11)$$

where $y_{t_i,i}$ denotes the prediction with estimated treatment $t_i \in \{0, 1\}$. y_i^* and t_i^* are the observations. The ATE is taken over all subjects. From [Greenland et al., 1999], these metrics cannot be properly estimated if there are confounding variables in the system. On the other hand, Pearl [Pearl, 1995a] introduces the “do-operator” [Pearl, 2019] on treatment to study this problem under intervention. The do symbol removes the treatment t from the given mechanism and sets it to a specific value by some external intervention. The notation $P(y|do(t))$ denotes the probability of y with possible interventions on treatment. Following Pearl’s back-door adjustment formula [Pearl, 2009] and the CGM in Fig. 1, it is proved in [Louizos et al., 2017] that the causal effect for a given binary treatment t , a proxy variable x , an outcome y and a confounding variable z can be evaluated by (similarly for $t = 0$):

$$p(y|x, do(t = 1)) = \int_z p(y|x, t = 1, z)p(z|x)dz \quad (12)$$

To intervene the information of t ($do(t)$), flipping errors [Louizos et al., 2017] with different rates (see **supplement C**) are applied to change the t_i label(s) [Paszke et al., 2017] in our experiments in Section 5.1. The proposed CGM and its associated TLT show resilient ATE estimation under statistical refutations.

Visual Patterns in the Intervention Level (III). We clarify two common scenarios, noisy context and under perturbation, in the intervention level (III) for noisy image classification. As shown in Tab. 2, the treatment information (t) is binary with an accessible noisy input x and **inaccessible** ontological (clean) representation \tilde{x} from Eq. (1) for visual pattern modeling. Next, we introduce datasets in the regime of the case 1 and 2 for our experiments in this work.

4.2 Case 1: NICO Dataset with Noisy Extra Visual Patterns

NICO [He et al., 2020] is a large-scale and open-access benchmark dataset for noisy image classification, which is motivated by studying non-independent image classification with causal modeling. The NICO dataset labels images with both main concepts (e.g., “cat”) and contexts as sub-labels (e.g., “water”). NICO is constructed by two super-classes: “animal” and “vehicle”, with 10 classes for “animal” and 9 classes for “vehicle”. In total, NICO contains 19 classes, 188 contexts, and 25,000 images. The design intuition of NICO is to provide a causal modeling benchmark for large-scale image classification. The authors evaluate several major image classification dataset (e.g., ImageNet, Pascal, and MS-COCO) and found out the auxiliary context information (treatment) is much random and inaccurate from statistical measurement for structuring validated causal inference. By selecting different contexts of the concept, testing data distribution can be unknown and different from training data distribution, which can be used to evaluate a causal inference model.

In our experiments, we follow the standard NICO evaluation process [He et al., 2020], where a concept is incorporated with two contexts. We further use **context** as treatment in the intervention level as in **Case 1** of Tab. 2. One context is the attribute of concept ($t = 1$) while another context is the background or scene of a concept ($t = 0$).

4.3 Case 2: Curated Causal Pairs (CPS) Dataset with Additive Artificial Noises

Despite many efforts in providing benchmark datasets for causal inference on non-vision tasks [Hill, 2011, LaLonde, 1986, Hoyer et al., 2009, Peters et al., 2014], visual causal data collection is relatively limited to bare causal effect evaluation with conditional visual treatments [Lopez-Paz et al., 2017]. Motivated by the perturbation-based causation studies testing biological network and the efforts from NICO, we further curate two datasets from public sources, named causal pairs (**CPS**), by using a diverse set of image perturbation types as treatment (i.e., **Case 2** in Tab. 2).

We select two representative datasets, Microsoft COCO [Lin et al., 2014], and a medicine dataset, Decathlon [Simpson et al., 2019], to create our CPS datasets. Each CPS contains pairs of original and perturbed images, as well as **five** different perturbation types described in Sec. 4.4. Table. 3 summarizes the NICO and our CPS datasets. Next, we introduce how to generate noisy images in CPS.

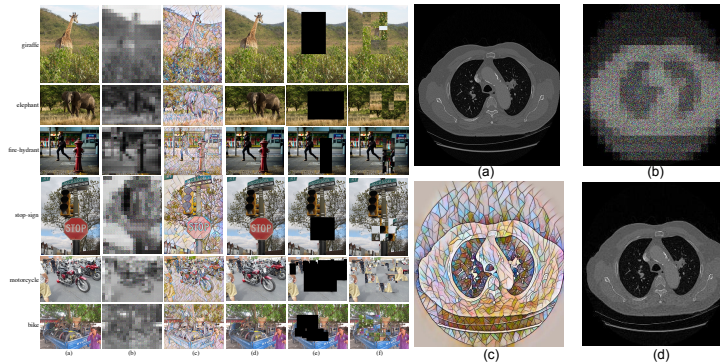


Figure 3: Illustration of our generated **CPS** dataset for noisy image classification. We randomly selected 50% of labeled images from both datasets and applied visual modifications to generate interventional observations. We selected similar object classes by 1,000 human surveys. *Left*: three causal pairs – giraffe/elephant, fire-hydrant/stop-sign, and motorcycle/bike. From left to right in **CPS**, the visual treatments are: (a) original input image, (b) image scrambling, (c) neural style transfer; (d) adversarial example. We further discuss masking intervention effects used in [Lopez-Paz et al., 2017, Yang et al., 2019] on general subjects by (e) object masking; and (f) background refilling. *Right*: a demonstration of Lung Tumours in Decathlon of the same format.

Table 3: Comparison of noisy image classification datasets: CPS with perturbation as a treatment (see Sec. 4.4) and NICO with noisy context (e.g., “indoor”).

Dataset	Treatment (Binary Information)	Numbers	Super-classes	Total classes
CPS (ours)	Receiving artificial noise (or not)	13,752	General / Medical	16
NICO	Existing context-wise pattern (or not)	25,000	Animal / Vehicle	19

Super-class 1: Generating Noisy General Objects. To generate CPS dataset from MS-COCO [Lin et al., 2014] for general super-class, we selected **six** similar object classes that could possibly result in confusing interpretation and recognition by human psychology studies [Reed, 2012, Musen and Treisman, 1990] (e.g., giraffe and elephant, etc.). We conduct a survey with 1,000 volunteers from Amazon mechanical turk [Turk, 2012] and pick the top-3 similarity label pairs. Specifically, we format three different common causal pairs, namely giraffe-elephant (CPS_1) with 3316 images, stop sign-fire hydrant (CPS_2) with 2419 images, and bike-motorcycle (CPS_3) with 4729 images, where the dataset is visualized in Fig. 3 (a).

Super-class 2: Generating Noisy Medical Images. For the medical super-class, we use an identical setting with 2630 training and 658 test CT images for **ten** different types (total classes) of human disease from Decathlon [Simpson et al., 2019], which includes: (1) Liver Tumours; (2) Brain Tumours; (3) Hippocampus; (4) Lung Tumours; (4) Prostate; (5) Cardiac; (6) Pancreas Tumour; (7) Colon Cancer; (8) Hepatic Vessels, and (10) Spleen. More details and visualization (Fig. 3 (b)) about this dataset are given in **supplement B**. From these two super-classes, we randomly selected 50% of these labeled images and applied visual modifications to generate interventional observations. Each generated image is assigned with a binary treatment indicator vector t_i , where its i -th element denotes the binary treatment label according to the i -th visual modification.

Table 4: Perturbation (e.g., texture) effects with classification accuracy (%) on the average of **CPS** images ($\sim 13.7k$) for different treatments and their causal effect estimates. Note that TLT (7.39M) has similar parameters compared with CVAE’ and CEVAE’, which are enhanced by ResNet as discussion in the ablation studies. **n** is for treatment noise level.

Type of t (with n = 0.05)	Classification Accuracy (\uparrow)			Average Treatment Effect (\uparrow)		
	CVAE’	CEVAE’	TLT (ours)	CVAE’	CEVAE’	TLT (ours)
Original (without t)	83.31 \pm 0.12	83.31 \pm 0.23	83.31 \pm 0.13	0.012	0.018	0.032
Style Transfer (ST)	73.67 \pm 0.31	74.34 \pm 0.26	76.12 \pm 0.27	0.354	0.343	0.318
Image Scrambling (IS)	72.31 \pm 1.27	76.21 \pm 0.81	80.12 \pm 0.54	0.057	0.295	0.288
Adversarial Example (AE)	79.12 \pm 0.25	81.12 \pm 0.17	83.12 \pm 0.12	0.025	0.027	0.036
Object Masking (OM)	70.12 \pm 0.19	72.73 \pm 0.21	73.06 \pm 0.11	0.179	0.241	0.243
Background Refilling (BR)	71.32 \pm 0.28	72.59 \pm 0.29	73.91 \pm 0.17	0.213	0.221	0.238

4.4 Visual Perturbation (Treatment) in CPS

We employ five distinct types of image modification methods as independent intervention variables: (i) image scrambling; (ii) neural style transfer; (iii) adversarial example; (iv) object masking, and (v) object-segment background shifting. Below we provide brief descriptions for these visual treatments as illustration in Fig. 3. **Image Scrambling (IS)** [Ye, 2010] algorithms re-align all pixels in an image to different positions to permute an original image into a new image, which is used in privacy-preserved classification [Tarr and Bülthoff, 1998].

Neural Style Transfer (ST) [Gatys et al., 2015] creates texture effect with perceptual loss [Johnson et al., 2016] and super-resolution along with instance normalization [Ulyanov et al., 2016].

Adversarial Example (AE) adds input perturbation for prediction evasion. We employ the Fast Gradient Sign Method (FGSM) [Goodfellow and Jones, 2015] with a scaled ℓ_∞ perturbation bound of $\epsilon = 0.3$. We also evaluated other attacks including C&W [Carlini and Wagner, 2017] and PGD [Madry et al., 2017] in **supplement B**.

Object Masking (OM) & Background Refilling (BR): Object masking (OM) was proposed in previous studies [Lopez-Paz et al., 2017, Yang et al., 2019] for causal learning. We applied OM and another masking methods, background refilling (BR), that duplicates non-object background into the mask segment as treatments.

5 Experiments

5.1 Noisy Image Classification on NICO and CPS

Generative Model Baselines

For a fair comparison, we select two benchmark conditional generative model incorporating both information of label (y) and binary treatment (t): modified conditional VAE [Sohn et al., 2015, Kingma and Welling, 2013] (CVAE’) and modified CEVAE [Louizos et al., 2017] (CEVAE’), where CVAE’ use $p(t, y)$ for concatenation as a conditional inference and CEVAE’ follows a similar causal variational inference process [Louizos et al., 2017] without features fusion and conditional queries. Both model are enhanced by ResNet [He et al., 2016] and attention layers with similar parameters (7.1M) with TLT. Noted CEVAE [Louizos et al., 2017] is originally designed and applied only on linear regression tasks but benefited from our causal modeling for noisy image classification.

Performance on NICO Dataset. We first evaluate models performance trained on NICO dataset. From the reported results in the paper [He et al., 2020, Zhang et al., 2021], we select the best reported model, StableNet from [Zhang et al., 2021] with sample weighting. As shown in Table. 5, generative models with proposed causal modeling attain competitive results on NICO with compositional bias setup, where TLT attains a best performance of **65.98%**. We provide more analysis under different setup of NICO, where TLT remains as the best model in **supplement C**.

Table 5: Classification accuracy (%) on NICO.

Model	StableNet [He et al., 2020]	CVAE’	CEVAE’	TLT
Acc.	59.76 \pm 1.52	57.23 \pm 2.12	62.17 \pm 1.82	65.98 \pm 1.74

Performance on CPS Dataset. In Table 4, we compare TLT with modified CVAE’ and modified CEVAE’ as baselines trained on **CPS** dataset. The accuracy of TLT in the original image, IS, ST, AE, OM and BR settings are consistently better than CVAE’ and CEVAE’, with substantially large margins ranging from **1.60%** to **7.81%**. CEVAE’ and TLT are also shown to have higher causal estimate (CE) than CVAE’ in all settings except for ST. Interestingly, ST leads to a higher causal value (from **0.318** to **0.354**) when compared to the other modifications such as IS and AT. This finding accords to the recent studies on DNN’s innate bias of using edges and textures for vision task [Geirhos et al., 2019]. CEVAE’ and TLT having lower value in ST setting could be explained by a more unbiased representation learned by inference network with lower dependency on edges and textures. A benchmark visualization of Guided Grad-CAM

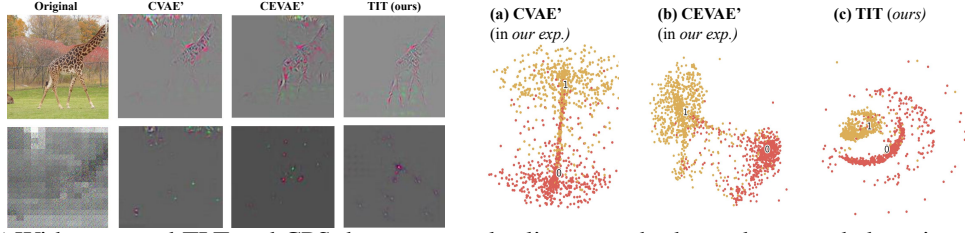


Figure 4: (a) With proposed TLT and CPS dataset, neural saliency methods can be extended to visual pattern from inference. Take the top row as an example, using TLT, guided grad-CAM [Selvaraju et al., 2017] can be more aligned with the concise human-interpretable giraffe patterns instead of forest texture and edges. More correlation analyses between saliency and labels in NICO and CPS are given in supplement C. (b) Visualization of learned manifolds of $q(z)$ by tSNE [Maaten and Hinton, 2008], proposed CTR’s results largest intra-cluster pair-wise sample distances between additive noise (adversarial) ($t = 1$) and vanilla ($t = 0$) image samples from CPS_1 .

[Selvaraju et al., 2017] in Fig. 4 (a) validates this hypothesis and highlights the importance of our inference network in gaining robust visual understanding from latent space z as tSNE [Maaten and Hinton, 2008] results Fig. 4 (b). One critical issue for visual intervention is its difficulty in investigating the effect on object mask size [Lopez-Paz et al., 2017, Pickup et al., 2014]. **supplement C** shows a consistent and stable performance of TLT against varying mask sizes.

Case Study on the medical super-class: We conduct the same experiments with medical super-class to identify visual clinical features. Both the classification and estimation performance are consistent with general CPS objects, where TLT attains the highest accuracy 88.74% in the original setting and 82.57% in the scrambling setting (e.g., data encryption operation) settings. TLT is most effective in classifying noisy image and more sensible in measuring ATE on adversarial example. We also conduct expert evaluation on the activation saliency of clinical patterns (Fig. 4). Based on their domain knowledge [Wang et al., 2017, Rajpurkar et al., 2017a,b], three physicians independently and unanimously give the highest confidence scores on saliency attributes to our method.

Statistical Refutation of Causal Models: To rigorously validate our ATE estimation result, we follow a standard refuting setting [Rothman and Greenland, 2005, Pearl et al., 2016, Pearl, 1995b] with the causal model in Fig. 1 to run three major tests, as reported in **supplement E** and Table S15, which validate our method is robust.

6 Conclusion

Motivated by human-inspired attention mechanism and causal hierarchy theorem, in this paper we proposed a novel framework named treatment learning transformer (TLT) for tackling noisy image classification with treatment estimation. In addition to showing significantly improved accuracy of TLT on the NICO dataset with noisy contexts, we also curated a new causal-pair dataset (CPS) based on five different visual image perturbation types for performance benchmarking on general and medical images. We validated the causal effect of TLT through statistical refutation testing on average treatment effects. We also show derived advantages of TLT in terms of improved visual saliency maps and representation learning. Our results suggest promising means and a new neural network architecture toward the advancement of research in the intersection of deep learning and visual causal inference.

References

- Olaf Ronneberger, Philipp Fischer, and Thomas Brox. U-net: Convolutional networks for biomedical image segmentation. In *International Conference on Medical image computing and computer-assisted intervention*, pages 234–241. Springer, 2015.
- Kaiming He, Xiangyu Zhang, Shaoqing Ren, and Jian Sun. Deep residual learning for image recognition. In *Proceedings of the IEEE conference on computer vision and pattern recognition*, pages 770–778, 2016.
- Gao Huang, Zhuang Liu, Laurens Van Der Maaten, and Kilian Q Weinberger. Densely connected convolutional networks. In *Proceedings of the IEEE conference on computer vision and pattern recognition*, pages 4700–4708, 2017.
- Judea Pearl. The seven tools of causal inference, with reflections on machine learning. *Communications of the ACM*, 62(3):54–60, 2019.

- Michael A Alcorn, Qi Li, Zhitao Gong, Chengfei Wang, Long Mai, Wei-Shinn Ku, and Anh Nguyen. Strike (with) a pose: Neural networks are easily fooled by strange poses of familiar objects. In *Proceedings of the IEEE Conference on Computer Vision and Pattern Recognition*, pages 4845–4854, 2019.
- Tong Xiao, Tian Xia, Yi Yang, Chang Huang, and Xiaogang Wang. Learning from massive noisy labeled data for image classification. In *Proceedings of the IEEE conference on computer vision and pattern recognition*, pages 2691–2699, 2015.
- Ian J Goodfellow, Jonathon Shlens, and Christian Szegedy. Explaining and harnessing adversarial examples. *ICLR*, 2015.
- Yue He, Zheyang Shen, and Peng Cui. Towards non-iid image classification: A dataset and baselines. *Pattern Recognition*, page 107383, 2020.
- Judea Pearl. Causal diagrams for empirical research. *Biometrika*, 82(4):669–688, 1995a.
- Jonas Peters, Joris M Mooij, Dominik Janzing, and Bernhard Schölkopf. Causal discovery with continuous additive noise models. *The Journal of Machine Learning Research*, 15(1):2009–2053, 2014.
- Christos Louizos, Uri Shalit, Joris M Mooij, David Sontag, Richard Zemel, and Max Welling. Causal effect inference with deep latent-variable models. In *Advances in Neural Information Processing Systems*, pages 6446–6456, 2017.
- Christine Trampusch and Bruno Palier. Between x and y : how process tracing contributes to opening the black box of causality. *New political economy*, 21(5):437–454, 2016.
- Judea Pearl, Madelyn Glymour, and Nicholas P Jewell. *Causal inference in statistics: A primer*. John Wiley & Sons, 2016.
- Maxime Oquab, Leon Bottou, Ivan Laptev, and Josef Sivic. Learning and transferring mid-level image representations using convolutional neural networks. In *Proceedings of the IEEE conference on computer vision and pattern recognition*, pages 1717–1724, 2014.
- Kihyuk Sohn, Honglak Lee, and Xinchen Yan. Learning structured output representation using deep conditional generative models. In *Advances in neural information processing systems*, pages 3483–3491, 2015.
- Jiangfan Han, Ping Luo, and Xiaogang Wang. Deep self-learning from noisy labels. In *Proceedings of the IEEE International Conference on Computer Vision*, pages 5138–5147, 2019.
- Yuncheng Li, Jianchao Yang, Yale Song, Liangliang Cao, Jiebo Luo, and Li-Jia Li. Learning from noisy labels with distillation. In *Proceedings of the IEEE International Conference on Computer Vision*, pages 1910–1918, 2017.
- Yarin Gal, Riashat Islam, and Zoubin Ghahramani. Deep bayesian active learning with image data. *arXiv preprint arXiv:1703.02910*, 2017.
- Xingxuan Zhang, Peng Cui, Renzhe Xu, Linjun Zhou, Yue He, and Zheyang Shen. Deep stable learning for out-of-distribution generalization. *arXiv preprint arXiv:2104.07876*, 2021.
- Jiashuo Liu, Zheyang Shen, Peng Cui, Linjun Zhou, Kun Kuang, Bo Li, and Yishi Lin. Stable adversarial learning under distributional shifts. *Proceedings of the AAAI Conference on Artificial Intelligence*, 2021.
- Lyndsey C Pickup, Zheng Pan, Donglai Wei, YiChang Shih, Changshui Zhang, Andrew Zisserman, Bernhard Scholkopf, and William T Freeman. Seeing the arrow of time. In *Proceedings of the IEEE Conference on Computer Vision and Pattern Recognition*, pages 2035–2042, 2014.
- Amy Fire and Song-Chun Zhu. Learning perceptual causality from video. *ACM Transactions on Intelligent Systems and Technology (TIST)*, 7(2):23, 2016.
- Karel Lebeda, Simon Hadfield, and Richard Bowden. Exploring causal relationships in visual object tracking. In *Proceedings of the IEEE International Conference on Computer Vision*, pages 3065–3073, 2015.
- Amy Fire and Song-Chun Zhu. Using causal induction in humans to learn and infer causality from video. In *Proceedings of the Annual Meeting of the Cognitive Science Society*, volume 35, 2013.
- David Lopez-Paz, Robert Nishihara, Soumith Chintala, Bernhard Scholkopf, and Léon Bottou. Discovering causal signals in images. In *Proceedings of the IEEE Conference on Computer Vision and Pattern Recognition*, pages 6979–6987, 2017.
- Murat Kocaoglu, Christopher Snyder, Alexandros G Dimakis, and Sriram Vishwanath. Causalgan: Learning causal implicit generative models with adversarial training. *arXiv preprint arXiv:1709.02023*, 2017.
- Mohammad Taha Bahadori, Krzysztof Chalupka, Edward Choi, Robert Chen, Walter F Stewart, and Jimeng Sun. Causal regularization. *arXiv preprint arXiv:1702.02604*, 2017.

- Chao-Han Huck Yang, Yi-Chieh Liu, Pin-Yu Chen, and Xiaoli Ma. When causal intervention meets image masking and adversarial perturbation for deep neural networks. *arXiv preprint arXiv:1902.03380*, 2019.
- Kaihua Tang, Yulei Niu, Jianqiang Huang, Jiaxin Shi, and Hanwang Zhang. Unbiased scene graph generation from biased training. In *Proceedings of the IEEE/CVF Conference on Computer Vision and Pattern Recognition*, pages 3716–3725, 2020.
- Jiaxin Qi, Yulei Niu, Jianqiang Huang, and Hanwang Zhang. Two causal principles for improving visual dialog. In *Proceedings of the IEEE/CVF Conference on Computer Vision and Pattern Recognition*, pages 10860–10869, 2020.
- Vedika Agarwal, Rakshith Shetty, and Mario Fritz. Towards causal vqa: Revealing and reducing spurious correlations by invariant and covariant semantic editing. In *Proceedings of the IEEE/CVF Conference on Computer Vision and Pattern Recognition*, pages 9690–9698, 2020.
- Ehsan Abbasnejad, Damien Teney, Amin Parvaneh, Javen Shi, and Anton van den Hengel. Counterfactual vision and language learning. In *Proceedings of the IEEE/CVF Conference on Computer Vision and Pattern Recognition*, pages 10044–10054, 2020.
- Dong Zhang, Hanwang Zhang, Jinhui Tang, Xian-Sheng Hua, and Qianru Sun. Causal intervention for weakly-supervised semantic segmentation. *Advances in Neural Information Processing Systems*, 33, 2020.
- Krzysztof Chalupka, Pietro Perona, and Frederick Eberhardt. Visual causal feature learning. *arXiv preprint arXiv:1412.2309*, 2014.
- Peter Bühlmann, Jonas Peters, Jan Ernest, et al. Cam: Causal additive models, high-dimensional order search and penalized regression. *The Annals of Statistics*, 42(6):2526–2556, 2014.
- Ricardo Pio Monti, Kun Zhang, and Aapo Hyvärinen. Causal discovery with general non-linear relationships using non-linear ica. In *Uncertainty in Artificial Intelligence*, pages 186–195. PMLR, 2020.
- Danilo Jimenez Rezende, Shakir Mohamed, and Daan Wierstra. Stochastic backpropagation and approximate inference in deep generative models. In *Proceedings of the 31st International Conference on International Conference on Machine Learning-Volume 32*, pages II–1278, 2014.
- Uri Shalit, Fredrik D Johansson, and David Sontag. Estimating individual treatment effect: generalization bounds and algorithms. In *Proceedings of the 34th International Conference on Machine Learning-Volume 70*, pages 3076–3085. JMLR. org, 2017.
- Diederik P Kingma and Max Welling. Auto-encoding variational bayes. *arXiv preprint arXiv:1312.6114*, 2013.
- Chao-Han Huck Yang, I Hung, Te Danny, Yi Ouyang, and Pin-Yu Chen. Causal inference q-network: Toward resilient reinforcement learning. *arXiv preprint arXiv:2102.09677*, 2021.
- Guido W Imbens and Donald B Rubin. Rubin causal model. In *Microeconometrics*, pages 229–241. Springer, 2010.
- Donald B Rubin. Estimating causal effects of treatments in randomized and nonrandomized studies. *Journal of educational Psychology*, 66(5):688, 1974.
- Judea Pearl. *Causality*. Cambridge university press, 2009.
- E Bareinboim, JD Correa, D Ibeling, and T Icard. On pearl’s hierarchy and the foundations of causal inference. *ACM Special Volume in Honor of Judea Pearl (provisional title)*, 2020.
- Ilya Shpitser and Judea Pearl. Complete identification methods for the causal hierarchy. *Journal of Machine Learning Research*, 9(Sep):1941–1979, 2008.
- Hareesh Bahuleyan, Lili Mou, Olga Vechtomova, and Pascal Poupart. Variational attention for sequence-to-sequence models. In *Proceedings of the 27th International Conference on Computational Linguistics*, pages 1672–1682, 2018.
- Ashish Vaswani, Noam Shazeer, Niki Parmar, Jakob Uszkoreit, Llion Jones, Aidan N Gomez, Łukasz Kaiser, and Illia Polosukhin. Attention is all you need. In *Advances in neural information processing systems*, pages 5998–6008, 2017.
- Paul W Holland. Statistics and causal inference. *Journal of the American statistical Association*, 81(396):945–960, 1986.
- Meike Nauta, Doina Bucur, and Christin Seifert. Causal discovery with attention-based convolutional neural networks. *Machine Learning and Knowledge Extraction*, 1(1):312–340, 2019.
- Tianwen Chen, Lars Michels, Kaustubh Supekar, John Kochalka, Srikanth Ryali, and Vinod Menon. Role of the anterior insular cortex in integrative causal signaling during multisensory auditory–visual attention. *European Journal of Neuroscience*, 41(2):264–274, 2015.

- Hubert Ramsauer, Bernhard Schöfl, Johannes Lehner, Philipp Seidl, Michael Widrich, Lukas Gruber, Markus Holzleitner, Milena Pavlović, Geir Kjetil Sandve, Victor Greiff, et al. Hopfield networks is all you need. *arXiv preprint arXiv:2008.02217*, 2020.
- Sander Greenland, James M Robins, Judea Pearl, et al. Confounding and collapsibility in causal inference. *Statistical science*, 14(1):29–46, 1999.
- Adam Paszke, Sam Gross, Soumith Chintala, Gregory Chanan, Edward Yang, Zachary DeVito, Zeming Lin, Alban Desmaison, Luca Antiga, and Adam Lerer. Automatic differentiation in pytorch. 2017.
- Jennifer L Hill. Bayesian nonparametric modeling for causal inference. *Journal of Computational and Graphical Statistics*, 20(1):217–240, 2011.
- Robert J LaLonde. Evaluating the econometric evaluations of training programs with experimental data. *The American economic review*, pages 604–620, 1986.
- Patrik O Hoyer, Dominik Janzing, Joris M Mooij, Jonas Peters, and Bernhard Schölkopf. Nonlinear causal discovery with additive noise models. In *Advances in neural information processing systems*, pages 689–696, 2009.
- Tsung-Yi Lin, Michael Maire, Serge Belongie, James Hays, Pietro Perona, Deva Ramanan, Piotr Dollár, and C Lawrence Zitnick. Microsoft coco: Common objects in context. In *European conference on computer vision*, pages 740–755. Springer, 2014.
- Amber L Simpson, Michela Antonelli, Spyridon Bakas, Michel Bilello, Keyvan Farahani, Bram van Ginneken, Annette Kopp-Schneider, Bennett A Landman, Geert Litjens, Bjoern Menze, et al. A large annotated medical image dataset for the development and evaluation of segmentation algorithms. *arXiv preprint arXiv:1902.09063*, 2019.
- Stephen K Reed. *Cognition: Theories and applications*. CENGAGE learning, 2012.
- Gail Musen and Anne Treisman. Implicit and explicit memory for visual patterns. *Journal of Experimental Psychology: Learning, Memory, and Cognition*, 16(1):127, 1990.
- Amazon Mechanical Turk. Amazon mechanical turk. Retrieved August, 17:2012, 2012.
- Guodong Ye. Image scrambling encryption algorithm of pixel bit based on chaos map. *Pattern Recognition Letters*, 31(5):347–354, 2010.
- Michael J Tarr and Heinrich H Bülthoff. Image-based object recognition in man, monkey and machine. *Cognition*, 67(1-2):1–20, 1998.
- Leon A Gatys, Alexander S Ecker, and Matthias Bethge. A neural algorithm of artistic style. *arXiv preprint arXiv:1508.06576*, 2015.
- Justin Johnson, Alexandre Alahi, and Li Fei-Fei. Perceptual losses for real-time style transfer and super-resolution. In *European conference on computer vision*, pages 694–711. Springer, 2016.
- Dmitry Ulyanov, Andrea Vedaldi, and Victor Lempitsky. Instance normalization: The missing ingredient for fast stylization. *arXiv preprint arXiv:1607.08022*, 2016.
- Michael Goodfellow and Amanda L Jones. Laceyella. *Bergey’s Manual of Systematics of Archaea and Bacteria*, pages 1–4, 2015.
- Nicholas Carlini and David Wagner. Adversarial examples are not easily detected: Bypassing ten detection methods. In *Proceedings of the 10th ACM Workshop on Artificial Intelligence and Security*, pages 3–14. ACM, 2017.
- Aleksander Madry, Aleksandar Makelov, Ludwig Schmidt, Dimitris Tsipras, and Adrian Vladu. Towards deep learning models resistant to adversarial attacks. *arXiv preprint arXiv:1706.06083*, 2017.
- Ramprasaath R Selvaraju, Michael Cogswell, Abhishek Das, Ramakrishna Vedantam, Devi Parikh, and Dhruv Batra. Grad-cam: Visual explanations from deep networks via gradient-based localization. In *2017 IEEE International Conference on Computer Vision (ICCV)*, pages 618–626. IEEE, 2017.
- Laurens van der Maaten and Geoffrey Hinton. Visualizing data using t-sne. *Journal of machine learning research*, 9(Nov):2579–2605, 2008.
- Robert Geirhos, Patricia Rubisch, Claudio Michaelis, Matthias Bethge, Felix A Wichmann, and Wieland Brendel. Imagenet-trained cnns are biased towards texture; increasing shape bias improves accuracy and robustness. *ICLR*, 2019.
- Xiaosong Wang, Yifan Peng, Le Lu, Zhiyong Lu, Mohammadhadi Bagheri, and Ronald Summers. Chestx-ray8: Hospital-scale chest x-ray database and benchmarks on weakly-supervised classification and localization of common thorax diseases. In *2017 IEEE Conference on Computer Vision and Pattern Recognition(CVPR)*, pages 3462–3471, 2017.

- Pranav Rajpurkar, Jeremy Irvin, Kaylie Zhu, Brandon Yang, Hershel Mehta, Tony Duan, Daisy Ding, Aarti Bagul, Curtis Langlotz, Katie Shpanskaya, et al. Chexnet: Radiologist-level pneumonia detection on chest x-rays with deep learning. *arXiv preprint arXiv:1711.05225*, 2017a.
- Pranav Rajpurkar, Jeremy Irvin, Aarti Bagul, Daisy Ding, Tony Duan, Hershel Mehta, Brandon Yang, Kaylie Zhu, Dillon Laird, Robyn L Ball, et al. Mura: Large dataset for abnormality detection in musculoskeletal radiographs. *arXiv preprint arXiv:1712.06957*, 2017b.
- Kenneth J Rothman and Sander Greenland. Causation and causal inference in epidemiology. *American journal of public health*, 95(S1):S144–S150, 2005.
- Judea Pearl. On the testability of causal models with latent and instrumental variables. In *Proceedings of the Eleventh conference on Uncertainty in artificial intelligence*, pages 435–443. Morgan Kaufmann Publishers Inc., 1995b.
- Jan Philipp Albrecht. How the gdpr will change the world. *Eur. Data Prot. L. Rev.*, 2:287, 2016.
- Bolei Zhou, Aditya Khosla, Agata Lapedriza, Aude Oliva, and Antonio Torralba. Learning deep features for discriminative localization. In *Proceedings of the IEEE Conference on Computer Vision and Pattern Recognition*, pages 2921–2929, 2016.
- Paul Downing, Jia Liu, and Nancy Kanwisher. Testing cognitive models of visual attention with fmri and meg. *Neuropsychologia*, 39(12):1329–1342, 2001.
- Steven J Luck, Geoffrey F Woodman, and Edward K Vogel. Event-related potential studies of attention. *Trends in cognitive sciences*, 4(11):432–440, 2000.
- Ute Leonards, Stefan Sunaert, Paul Van Hecke, and Guy A Orban. Attention mechanisms in visual search—an fmri study. *Journal of Cognitive Neuroscience*, 12(Supplement 2):61–75, 2000.
- Aaditya Prakash, Nick Moran, Solomon Garber, Antonella DiLillo, and James Storer. Deflecting adversarial attacks with pixel deflection. In *Proceedings of the IEEE Conference on Computer Vision and Pattern Recognition*, pages 8571–8580, 2018.
- Andrew Ilyas, Shibani Santurkar, Dimitris Tsipras, Logan Engstrom, Brandon Tran, and Aleksander Madry. Adversarial examples are not bugs, they are features. *arXiv preprint arXiv:1905.02175*, 2019.

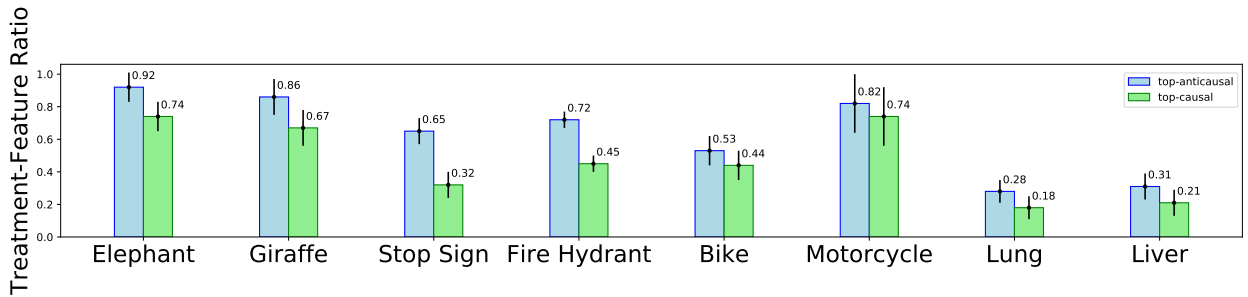
A The “What If” Challenges for Deep Neural Networks (DNNs)

A causal inferable DNNs for reasoning chaotic real-world patterns [Pearl, 2009, Yang et al., 2019, Pearl, 1995a] would be necessary for many practice scenarios. Recent regulatory concerns (e.g., GDPR [Albrecht, 2016]) on Artificial Intelligence (AI) safety and self-driving automobile accidents also highlight the importance and the emergence of understanding: (1) "What" does a DNNs model "learn for accurate label-prediction and (2) utilizing the "Why" relationship between labels generated by human knowledge and their conceptional pattern representations in the real world.

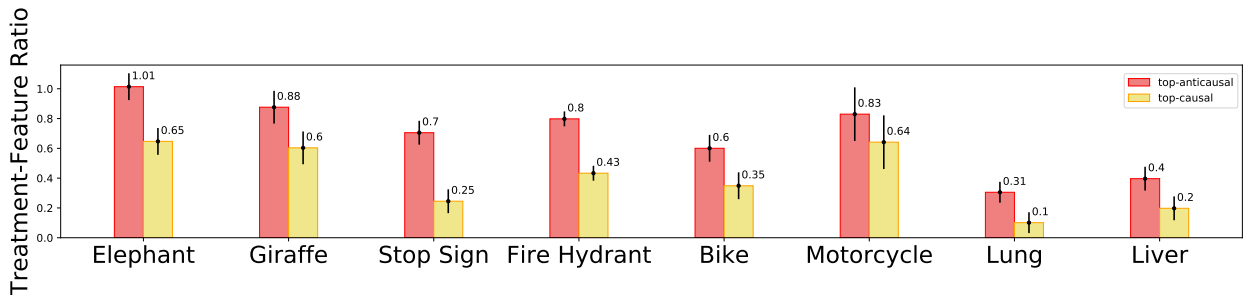
We propose $COCO_{CP}$ dataset based on MS-COCO [Lin et al., 2014]. $COCO_{CP}$ dataset includes classes having similar object(concept) but are different in context that could possibly result in confusing interpretation and recognition by human psychology studies (e.g., giraffe and elephant, etc.). In total, three different common causal pairs are formatted, namely giraffe-elephant (g-e) with 3316 images, stop sign-fire hydrant (s-f) with 2419 images, and bike-motorcycle (b-m) with 4729 images. A pair of stop sign and fire hydrant has been selected to study public awareness of on-road visual detection.

A.1 Neural Causation Coefficient (NCC)

Neural Causation Coefficient (NCC) [Lopez-Paz et al., 2017] is a novel observational causal discovery technique for the joint distribution of a pair of related proxy variables that are computed by applying CNNs to the image pixels. NCC leverages such embedded joint distribution as a regularization term to encourage the learning of causal or anticausal patterns in neural networks. Lopez et al. [Lopez-Paz et al., 2017] used an augmented NCC network to prove the existence of causal relations in ResNet [He et al., 2016] between object and context in an image, and showed that in object-feature ratio anticausal signal consistently has stronger relation than causal signal. However, they mainly focus on discussing the object-context causal hypothesis in the image setting, but barely covers the measurement of perturbation effect.



(a) TFR calculated by feature f_R from ResNet34 [He et al., 2016] as [Lopez-Paz et al., 2017].



(b) TFR calculated by feature f_C from our proposed CAN.

Figure 5: Evaluation of causal pairs by treatment feature ratio (TFR) score [Lopez-Paz et al., 2017]. The average and standard deviation of TFR associated to the top-1% causal/anticausal feature scores are displayed. The results show the visual perturbation measurement is coherent with the previous study [Lopez-Paz et al., 2017].

From Eq. 12, **object-feature ratio (OFR)** [Lopez-Paz et al., 2017] could be extended to a **treatment-feature ratio (TFR)** score s_i^t by do-operator [Pearl, 2019] as:

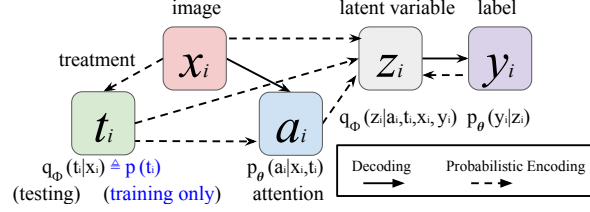


Figure 6: Generative process of Treatment Inference Transformer model. **Solid lines:** decoding phase. **Dashed lines:** probabilistic encoding phase. The treatment information could be only observed during training.

$$s_l^t = \frac{\sum_{j=1}^m |(f_{jl}^c | do(t)) - (f_{jl} | do(t))|}{\sum_{j=1}^m |(f_{jl} | do(t))|}, \quad (13)$$

where ($l=512$) is the input feature length, and f_j^t corresponding vectors of feature scores is equivalent to $F_{DNN}(x_j^t)$.

We reproduce the NCC architecture from [Lopez-Paz et al., 2017] and find all the anti-causal scores of COCO is larger than causal score as shown as [Lopez-Paz et al., 2017].

A.2 Correlation and Causation in Vision Task

Correlation [Pearl, 2009, 2019, 1995a] is a statistical measure that describes the size and direction of a relationship between two or more variables. A correlation between variables, however, does not automatically mean that the change in one variable is the cause of the difference in the values of the other variable. Causation [Pearl, 2019, 2009] indicates that one event is the result of the occurrence of the other event; i.e., there is a causal relationship between the two events. This is also referred to as cause and effect.

Theoretically, the difference between the two types of relationships are easy to identify — an action or occurrence can cause another (e.g., having rain droplet causes an increase in the risk of developing rain day), or it can correlate with another (e.g., a visual rain droplet is correlated with a red umbrella, but it does not lead to having a representation of a red umbrella in vision directly). In practice, however, it remains difficult to establish cause and effect, compared with establishing correlation clearly. Yet, most of the current deep learning method focused on directly visualizing the patterns after the visual model is trained without verifying (e.g., intervention methods [Pearl, 2019, Yang et al., 2019]) the causation between each representing patterns.

A.3 Basic Metrics for Causal Inference

By defining the CE of the individual treatment effect (ITE) as the difference between two potential outcomes for the individual [Louizos et al., 2017, Shalit et al., 2017], the average treatment effect (ATE) is defined as the expected value of the potential outcomes over the subjects.

B Dataset

B.1 Dataset Statistics: CPS General

In order to accurately measure visual causality, we select six categories from MS-COCO [Lin et al., 2014] and match them into three causal pairs, which are giraffe-elephant, bicycle-motorcycle, and stop sign-fire hydrant. Each pair is chosen by its matching characteristic and background and split into train and validation set by MS-COCO default setting. With similar characteristics, we are able to study on the causality of how network classifies different categories. To avoid network relying on texture to predict, every pair has a similar background, which makes our classifier more robust to evaluate the causal effect. Next, we analyze the properties of each pair and compare them. The number of images and instances per category for both train and validation set are shown in Fig.7 and Fig.8. In addition, the segmentation size of each pair is shown in Table.6. The segmentation size of each pair influence the performance of our classifier for excessive noise from background increasing the difficulty to find the correct hidden features as shown in Table.7.

B.2 Dataset Statistics: CPS Medical

In total, 2,633 three-dimensional images (with 658 test images) were collected across multiple anatomies of interest, multiple modalities, and multiple sources (or institutions) representative of real-world clinical applications followed by

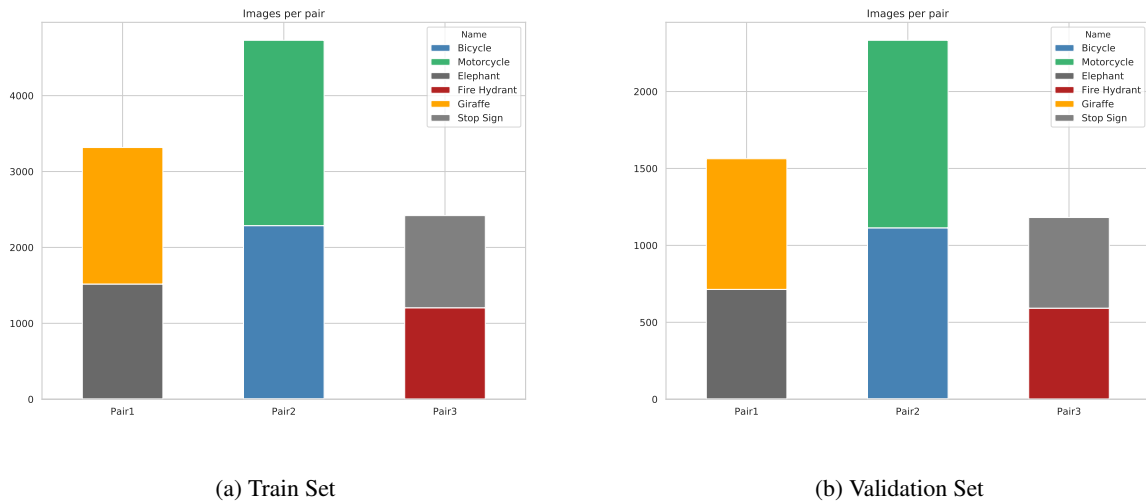


Figure 7: **Image** details per pairs in CPS: CPS_1 – Giraffe-Elephant, CPS_2 – Bicycle-Motorcycle, and CPS_3 – Stop sign-Fire hydrant.

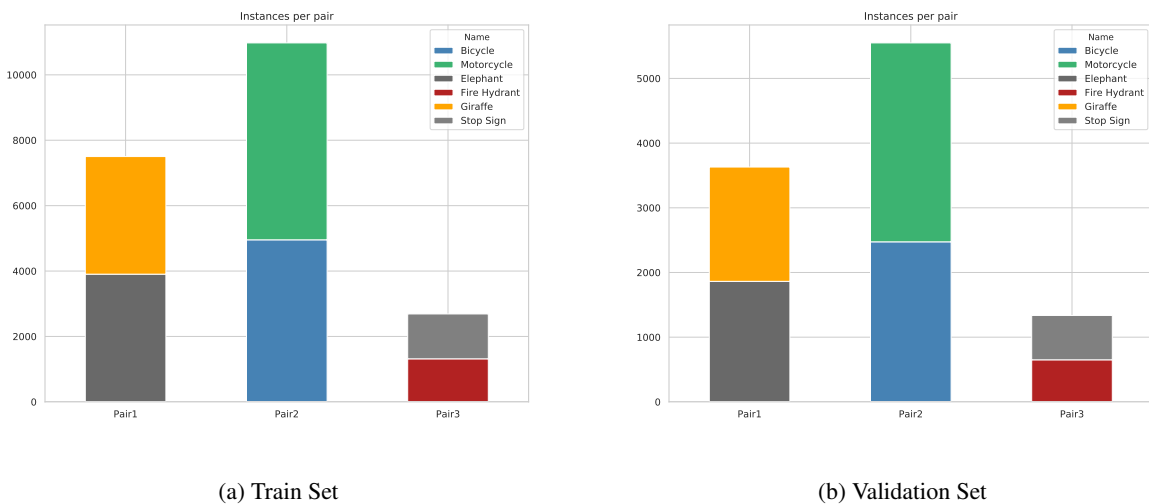


Figure 8: **Instance** details per pairs in CPS: CPS_1 – Giraffe-Elephant, CPS_2 – Bicycle-Motorcycle, and CPS_3 – Stop sign-Fire hydrant.

Table 6: Percentage of Segmentation in Images

Pair 1	Giraffe	Elephant
	14.60%	24.13%
Pair 2	Bicycle	Motorcycle
	5.74%	15.59%
Pair 3	Stop Sign	Fire Hydrant
	7.58%	7.64%

Table 7: **CPS General**: performance for common object [Lin et al., 2014] causal pairs with different visual treatments.

	Treatment	CVAE'	CEVAE _{att}	TIT
Bicycle & Motorcycle	Object Masking 0.0	78.31 ±0.17	80.79 ±0.06	81.05 ±0.11
	Object Masking 0.5	74.98 ±0.09	79.46 ±0.12	79.51 ±0.16
	Object Masking 1.0	71.65 ±0.23	72.85 ±0.13	73.29 ±0.08
	Background Refilling 0.5	75.28 ±0.15	77.5 ±0.27	78.68 ±0.20
	Background Refilling 1.0	71.11 ±0.42	74.49 ±0.38	73.95 ±0.41
Stop Sign & Fire Hydrant	Object Masking 0.0	74.59 ±0.29	75.79 ±0.26	77.41 ±0.19
	Object Masking 0.5	72.28 ±0.10	73.91±0.05	74.08 ±0.08
	Object Masking 1.0	68.67 ±0.34	71.22 ±0.28	71.06 ±0.24
	Background Refilling 0.5	69.13 ±0.16	73.79 ±0.21	75.45 ±0.14
	Background Refilling 1.0	65.62 ±0.47	66.65 ±0.37	68.24 ±0.44
Elephant & Giraffe	Object Masking 0.0	93.72 ±0.25	93.53 ±0.28	94.67 ±0.20
	Object Masking 0.5	90.14 ±0.11	93.01 ±0.19	93.15 ±0.09
	Object Masking 1.0	80.12 ±0.19	82.73 ±0.21	83.06 ±0.11
	Background Refilling 0.5	90.44 ±0.08	91.71 ±0.11	91.73 ±0.10
	Background Refilling 1.0	81.32 ±0.28	82.59 ±0.29	83.91 ±0.17

COCO-CP processing. All images were identified using processes consistent with institutional review board polices at each contributing site. We reformatted the images to reduce the need for specialized software packages for reading to encourage use by specialists in medical imaging for high-level feature reasoning.

Human Evaluation

Chest MRI can provide important features to diagnose lung problems such as a tumor or pleural disorder, blood vessel problems, or abnormal lymph nodes. We collaborate with three **board-certified thoracic surgeons** to review the activate region generated by guided grad-CAM [Selvaraju et al., 2017] on the test images. The surgeons individually retrospectively reviewed and labeled each study from the generated 100 image results as a DICOM file as consistent or inconsistent saliency compared with their diagnosis using the PACS system. The radiologists have averaged 6.43 years of experience on average, ranging from 5 to 16 years.

The TIT-generated saliency results also attain the highest consistency (61.2%) from thoracic surgeons compared with the results from VAE_{Res} (48.1%) and CEVAE_{Res}* (58.8%). The consistency from a randomly generated saliency map is only (3.2%).

B.3 Ablation Study

Starting from a ResNet, we modified the architecture towards proposed TIT and compare the accuracy performance of various architecture. Table. 9 shows the impact of each change of the architecture on COCO_{CP} classification. Among all variation, attention mechanism is the most important feature, while having bilinear fusion (BF) is also more effective than concatenation.

Table 8: Accuracy performance under adversarial attack as the treatment. TIT attains higher accuracy in both FGSM, C&W, and PGD settings.

Method	CVAE'	CEVAE'	TIT
FGSM [Goodfellow and Jones, 2015]	91.92±0.11	92.02±0.11	92.86 ±0.12
C&W [Carlini and Wagner, 2017]	82.32 ±2.34	74.23±4.18	88.12 ±1.26
PGD [Madry et al., 2017]	74.32 ±1.38	86.34±1.70	89.43 ±1.08

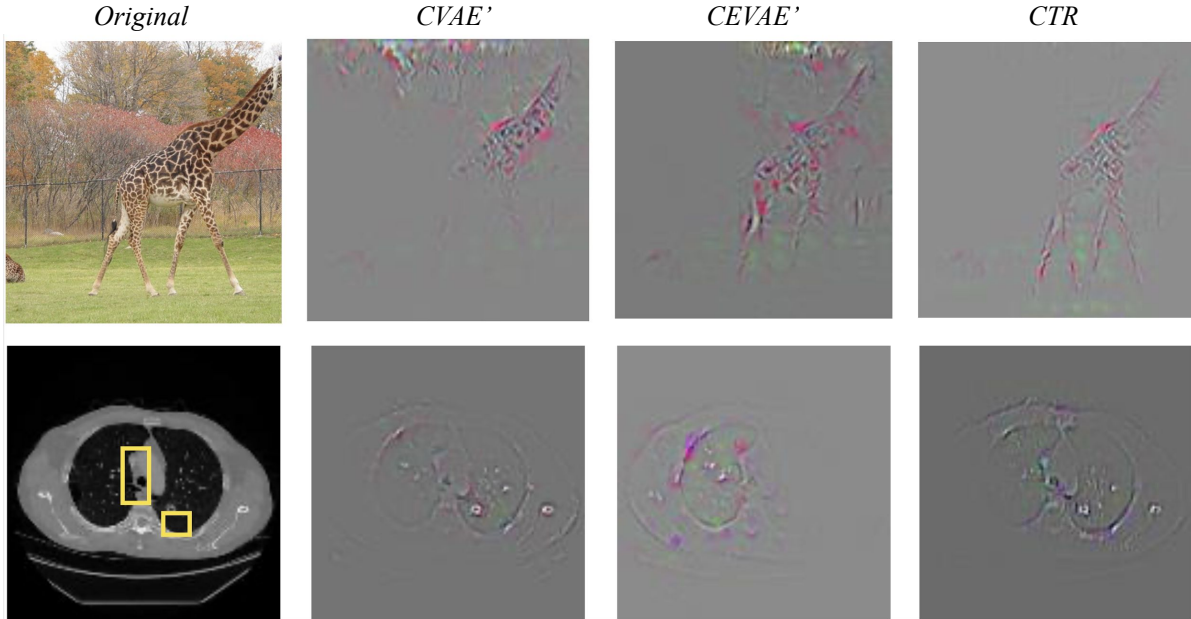


Figure 9: We use class activation mapping methods [Zhou et al., 2016, Selvaraju et al., 2017] to explain our medical classification model. The yellow bounding box is ground truth label from the Decathlon [Simpson et al., 2019] dataset. The guided-grad CAM method shows a highest false-negative scores on the region of interest.

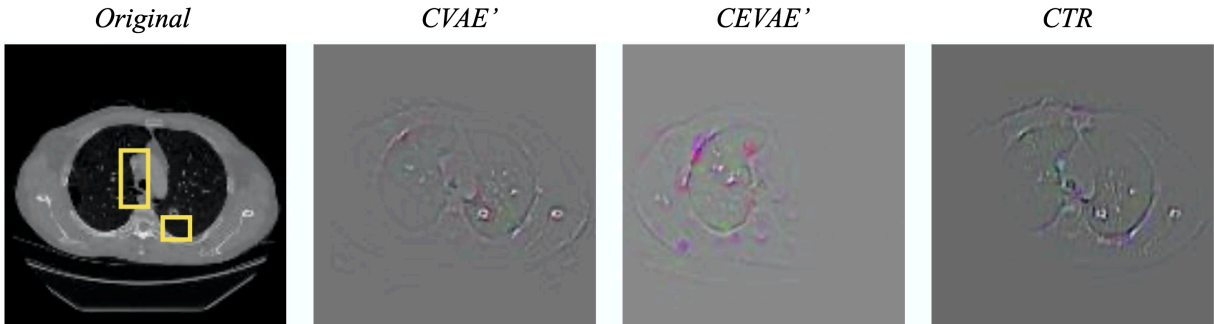


Figure 10: We show Guided-Grad-CAM results on different classification model. The results generated from CAM is much matching yellow bounding box from the Decathlon [Simpson et al., 2019] dataset in the test dataset.

C Parameter and Architecture

C.1 Adversarial Perturbation

With recent security concerns of adversarial example over visual recognition, we also made a broad study on the accuracy and causal effect under adversarial examples. Fast Gradient Sign Method (FGSM) [Goodfellow and Jones, 2015] is a classical gradient-based adversarial noise to generate adversarial examples by one step gradient update along the direction of the sign of gradient at each pixel by:

$$X_{\text{Adversarial}} = X + \varepsilon \cdot \text{sign}(\nabla_X J(X, Y)), \quad (14)$$

where J is the training loss (e.g. cross entropy) and Y is the groundtruth label for X . We adopt FGSM as an visual modification with $\varepsilon = 0.3 \ell_\infty$ perturbation constraint. This treatment could be further extended on other adversarial examples combined with causal analysis [Yang et al., 2019]. Instead of FGSM, we also study the accuracy performance under Carlini-Wagner attack (C&W) [Carlini and Wagner, 2017] and projected gradient descent (PGD) [Madry et al., 2017] as treatment. As shown in Table 8, our proposed TIT attains higher accuracy and less accuracy degradation in FGSM, C&W and PGD settings compared to CVAE' and CEVAE' for CPS classification.

C.2 Overparameterization

For a fair comparison, we study the performance of architectures with similar number of parameters. To align with the number of parameter in TIT, We modify the number of Resblocks in CVAE' as 4 and add attention mechanism to CEVAE'. As shown in Table 10, with similar number of parameters, our proposed TIT acquire the highest accuracy and better utilize the power of more parameters to compete with the state-of-art CVAE' architecture.

C.3 Different Mask Size

We study the effect of different mask sizes with same intervention flipping rate. The object-masking and background-refilling are used as visual perturbation in the experiments. To observe the effect, we gradually increased the mask ratio among the target object. The results in Table 12 and Table 14 show the impact of changing the ratio to the accuracy of CPS general and medical dataset classification. We find the accuracy drops as the ratio increasing, while our proposed TIT is relatively resilient to the high noise ratio scenario and perform better classification.

C.4 NICO Dataset Settings

NICO dataset provides several settings to simulate the Non-I.I.D dataset on different levels. 4 typical settings to generate Non-I.I.D training and testing subset.

Minimum Bias

The setting choose the images in target class as positive samples and images in other classes as negative samples ignoring the context, which could lead to a minimum distribution shift in training and testing subset.

Proportional Bias

The setting takes all context into consideration but the ratio of each context are different in training and testing subset. In this setting, the level of distribution shift can be adjusted based on the difference of context ratio.

Compositional Bias

In this setting, the contexts exist in test subset are not guaranteed to exist in training subset. The distribution shift is higher between training and testing set. The shift could be enhanced by adding proportional bias.

We carefully observe the effect of different settings imposing on different model. The result in Table. 11 shows our proposed TIT performs better in all settings compared to other models including the CNBB model proposed by [He et al., 2020].

Table 9: Model architecture ablation study in COCO_{CP}

Architecture	Val. Acc. (%)
ResNet	81.23±0.12
ResNet + CVAE = CVAE'	82.31±0.13
ResNet + CEVAE = CEVAE''	82.17±0.24
CEVAE + BF - bernoulli = CEVAE'	82.68±0.15
Treatment Inference Transformer (TIT)	84.32±0.07

Table 10: Overparameterization ablation study in COCO_{CP}

Model	Para.	Val. Acc. (%)
CVAE'	4.03M	82.31±0.13
CVAE' + 2 Resblocks	5.92M	82.38 ±0.18
CVAE' + 4 Resblocks	7.83M	81.96 ±0.19
CEVAE' + Attention _C	7.81M	83.62 ±0.21
TIT (ours)	7.39M	84.92±0.07

Table 11: Classification accuracy (%) on NICO dataset with different model and setting. Setting 1,2 and 3 refers to minimum bis, proportional bias and compositional bias mentioned in C separately.

Setting	CNBB [He et al., 2020]	CVAE'	CEVAE'	TIT
Setting 1	42.96 ±1.54	48.72 ±2.01	53.94 ±1.74	57.02 ±1.42
Setting 2	44.15 ±1.48	50.10 ±1.98	54.33 ±1.64	58.75 ±1.44
Setting 3	45.16 ±1.52	50.23 ±2.12	56.17 ±1.82	60.98 ±1.52

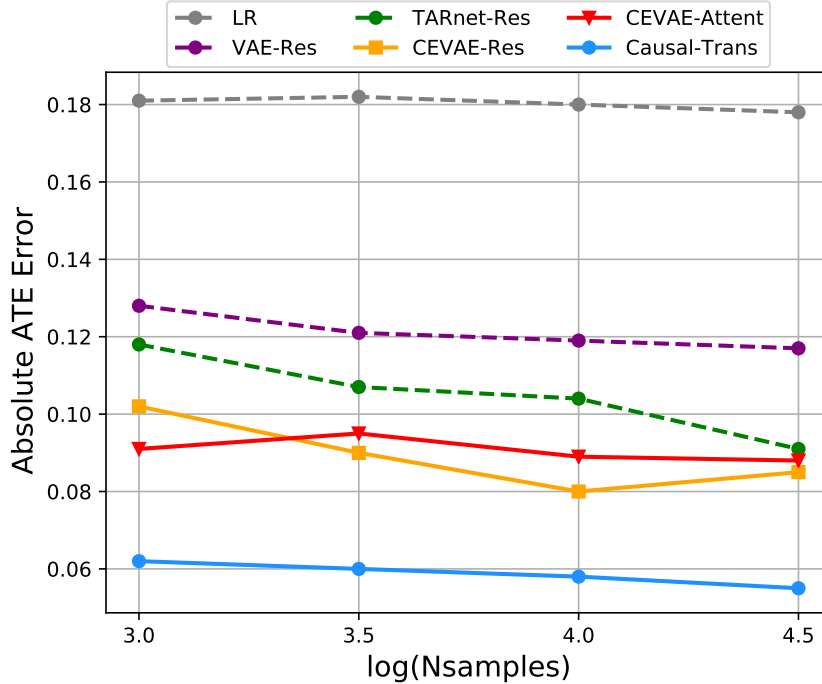


Figure 11: Error bar of average treatment effect

Table 12: Accuracy (%) of varying mask sizes when intervention flipping rate $\mathbf{n} = 0.05$. $\mathbf{I}_{OM}/\mathbf{I}_{BR}$ denotes Object-Masking/Background-Refilling. The number $X\%$ means masking $X\%$ of a target object. Our proposed method (TIT) maintains relatively high accuracy as X increases.

\mathbf{I}_{OM}	CVAE'	CEVAE _{att}	TIT	\mathbf{I}_{BR}	CVAE	CEVAE _{att}	TIT
10%	93.31 \pm 0.17	92.58 \pm 0.21	94.32 \pm 0.08	10%	93.04 \pm 0.16	94.25 \pm 0.18	94.65 \pm 0.09
30%	91.19 \pm 0.15	93.37 \pm 0.19	94.13 \pm 0.07	30%	91.27 \pm 0.21	93.53 \pm 0.23	94.25 \pm 0.11
50%	90.14 \pm 0.11	93.01 \pm 0.19	93.15 \pm 0.09	50%	90.44 \pm 0.08	91.71 \pm 0.11	91.73 \pm 0.10
70%	86.53 \pm 0.13	91.90 \pm 0.23	91.26 \pm 0.18	70%	86.62 \pm 0.21	88.85 \pm 0.18	90.46 \pm 0.12
100%	80.12 \pm 0.19	82.73 \pm 0.21	83.06 \pm 0.11	100%	81.32 \pm 0.28	82.59 \pm 0.29	83.91 \pm 0.17

D Reproducibility

D.1 Hyper-Parameters and Experiment Setup

Causal Effect Autoencoder[Louizos et al., 2017] (**CEVAE_{Res}***) baseline: To empower CEVAE for the visual data, our input images use $\dim(C)=3$, $\dim(X)=128$, $\dim(Y)=128$. The encoder part of VAE model utilized in paper takes the ResNet34 as feature extractor. Then we sample the $q(t|x)$ by Bernoulli distribution, and $q(y|x, t)$ and $q(z|x, y, t)$ are sampled by densely connected hidden layer of 512 neurons. Sequentially, the Z is generated by reparameterization from $q|t$. The decoder starts from 3 ResBlocks with 512 width for the $\dim(Z)=512$ to reconstruct the $p(x|z)$, we further used 5 upsample blocks with 2 times scaling up and convolution layers with [512,256,128,64,32] width. For the last convolution layer, we use reflection padding with width set as 3. Also, we sample the $p(t|z)$ and $p(y|t, z)$ by projecting t and $\mu_y(t)$ through adaptive pooling and the densely connected hidden layer with 512 width.

CEVAE with Attention baseline (CEVAE_{Att}): For a much fair comparison with proposed Treatment Inference Transformer (TIT), we apply the dual attention module in the encoder part of CEVAE to approximate the $q(z|x, t, y)$. The dual attention module consists of position and channel attention module.

- Global feature: After 1x1 convolution, the input is scaled by 4 times larger with bilinear interpolation.
- Position attention: The module outputs the position attention combined by 2 convolution layers with 64 width to calculate the attention.

- Channel attention: The module outputs the channel attention by fusing the channel into spatial information and pass the feature to 2 convolution layers with 64 width.
- Combination: The output has the channel of 512, the same width as the input.

The weights of the network are initialized with weights from a model pre-trained on ImageNet. The Adam algorithm with standard parameters and learning rate **0.001** are utilized for optimization. We use mini-batches of size 128 and pick the models with the highest accuracy. All experiments of our model are implemented in PyTorch using an NVIDIA GeForce GTX 2080 Ti GPU with 12GB memory. The training time for each MS-COCO [Lin et al., 2014] causal pair with different visual treatment takes one hour to two hours on average. The reproducible code of CAN networks and a causal graphical model have been provided in the supplementary and will be open source¹.

D.2 Cognitive Response to Attention Mechanism

Cognitive psychology and neuroimaging [Downing et al., 2001] studies have found a distinct neural response to the different visual scene, as the visual attention mechanism [Luck et al., 2000]. Attention exercises, Luck et al., [Luck et al., 2000] have been proved to be enhanced learning capacities by executive control and transferring to cognitive abilities. Since images from different categories vary systematically in their visual properties as well as their semantic category, variation in visual property may influence our cognitive process of visual stimuli. The human brain has the ability to distinguish the visual scenes from different categories when categorical perception is impaired. For example, scrambling and masking are used widely when experimenting with visual pattern sensitivity. Although these perturbation preserved many of their visual characteristics, perception of scene categories was severely impaired, which makes scrambling and masking suitable metrics to compare the visual perception process between neural network and the human brain. These experiments [Luck et al., 2000, Leonards et al., 2000] have been validate on adding attention training for a improved learning performance in human education.

D.3 Using Saliency Map to Associate Learned Causal Patterns

To better understand the learned causal patterns from **TIT**, we use class activation mapping [Zhou et al., 2016] (CAM) to study [Yang et al., 2019, Pearl, 2019, 2009, 1995a] the causal patterns. CAM removes all fully-connected layers at the end, and including a tensor product (followed by softmax), which takes as input the global-average-pooled convolutional feature maps, and outputs the probability for each class. To obtain the class-discriminative localization map, Grad-CAM computes the gradient of y_c (score for class c) with respect to feature maps \mathbf{A} and importance weights α_k^c of a convolutional layer. Similar to CAM, Grad-CAM [Selvaraju et al., 2017] heat-map is a weighted combination of feature maps, and followed by a ReLU:

$$L_{\text{GradCAM}}^c = \text{ReLU} \left(\sum_k \alpha_k^c A^k \right) \quad (15)$$

In our DNN visualization experiment, we use the state-of-the-are CAM method, guide-GradCAM [Selvaraju et al., 2017] for comparing CVAE', CEVAE', and our TIT. guided-GradCAM fuse guided backpropagation and the Grad-CAM visualizations via a point-wise multiplication.

Interestingly, according to the intervened image after class-activation mapping techniques in Fig. 4 in the main context and Fig. 12 in the supplementary, we could find out when the area of interest are much central on the texture and edge effect. To reduce the texture dependent variable, we utilize a neural style transfer on the image set before the intervention.

E Identification of Visual Causal Effect

E.1 Causality

Rubin's Causal Model (Sekhon, 2008) is a framework developed for the statistical analysis of cause of effect based on the idea of potential outcomes. Consider:

- t_i , a binary treatment \mathbf{t} for individual i with 1 referring to assigning the treatment and 0 to no treatment;
- y_i is the outcome on individual i given a treatment value.

Each individual can have two potential outcomes or (counterfactuals) available as $\{y_i(1), y_i(0)\}$ \mathbf{t} corresponding to receiving the treatment or not.

¹Please follow the readme in the supplementary open-source code for more information

Table 13: Refuting tests of the causal estimate [Pearl, 2019] with causal effect (CE) over different treatment. The validation tests show our method is confident since the common random selection (T_c) and Subset test (T_s) are closed to the original CE, and all the CE results after replacing treatment with a random (placebo) variable (T_p) are close to zero.

Treatment	Original ATE	Test-Common (T_c) \uparrow	Test-Placebo (T_p) \downarrow	Test-Subset (T_s) \uparrow
IS: TIT	0.288	0.288	0.00479	0.288
CEVAE _{att}	0.2948	0.2941637	0.0427	0.276
CVAE'	0.057	0.05673101	0.0385	0.0583
AT: TIT	0.036	0.035	0.012	0.035
CEVAE _{att}	0.027	0.0274	0.0062	0.024
CVAE'	0.0247	0.0242	0.01347	0.0156
SB: TIT	0.2334	0.23385	0.0253	0.238
CEVAE _{att}	0.2417	0.2431	0.0364	0.2353
CVAE	0.1853368	0.1853	0.01157	0.1834
IM: TIT	0.1855	0.1854	0.037	0.191
CEVAE _{att}	0.22	0.22	0.0038	0.1736
CVAE'	0.222	0.22285	0.0200707	0.1609
ST: TIT	0.31763	0.317641	0.0278	0.3351
CEVAE _{att}	0.3431	0.342221	0.0225	0.3252
CVAE'	0.354412	0.354334	0.01127	0.3257

Table 14: Classification accuracy (%) with error bars (with 10-fold cross-validation) comparison between different visual treatments under intervention in the **CPS** dataset.

Treatment	CVAE'	CEVAE _{att}	TIT
Object Masking 0.0	93.61 \pm 0.15	93.31 \pm 0.11	94.91 \pm 0.15
Object Masking 0.1	93.31 \pm 0.17	93.58 \pm 0.21	94.32 \pm 0.08
Object Masking 0.3	91.19 \pm 0.15	93.37 \pm 0.19	94.13 \pm 0.07
Object Masking 0.5	90.14 \pm 0.11	93.01 \pm 0.19	93.15 \pm 0.09
Object Masking 0.7	86.53 \pm 0.13	91.90 \pm 0.23	91.26 \pm 0.18
Object Masking 1.0	80.12 \pm 0.19	82.73 \pm 0.21	83.06 \pm 0.11
Background Refilling 0.1	93.04 \pm 0.16	94.25 \pm 0.18	94.65 \pm 0.09
Background Refilling 0.3	91.27 \pm 0.21	93.53 \pm 0.23	94.25 \pm 0.11
Background Refilling 0.5	90.44 \pm 0.08	91.71 \pm 0.11	91.75 \pm 0.10
Background Refilling 0.7	86.62 \pm 0.21	88.85 \pm 0.18	90.46 \pm 0.12
Background Refilling 1.0	81.32 \pm 0.28	82.59 \pm 0.29	83.91 \pm 0.17
Image Scrambling	59.42 \pm 2.19	77.3 \pm 1.17	78.8 \pm 0.62
Style Transfer	67.73 \pm 2.19	68.12 \pm 1.21	68.29 \pm 0.42
Adversarial Example	91.92 \pm 0.11	92.02 \pm 0.11	92.86 \pm 0.12

Identifying conceptional treatment effect Individual Treatment Effect (ITE) can be defined as the difference between the two potential outcomes for the individual; Average Treatment Effect (ATE) as the expected value of the potential outcomes over the subjects. For a binary outcome, it is defined as: given by:

$$y_i = y_i(0)(1 - t_i) + y_i(1)t_i; ATE = \mathbb{E}[y_i(1)] - \mathbb{E}[y_i(0)]; \quad (16)$$

$$\begin{aligned} y_i &= y_i(0)(1 - t_i) + y_i(1)t_i; \\ ATE &= \mathbb{E}[y_i(1)] - \mathbb{E}[y_i(0)]; \end{aligned} \quad (17)$$

The above mentioned metric cannot be properly estimated if there are confounding variables in the system, which will introduce bias (Greenland et al., 1999). The causal effect by a treatment variable t on an outcome y is represented by $E[y|do(t=1)]$, where do represents the fact that the treatment has been kept at a specific value by external interventions on the system which do not affect other variables and their causal relationships in the system. Pearl defines the causal effect for a given treatment t and an outcome y and other confounding variables \mathbf{Z} as:

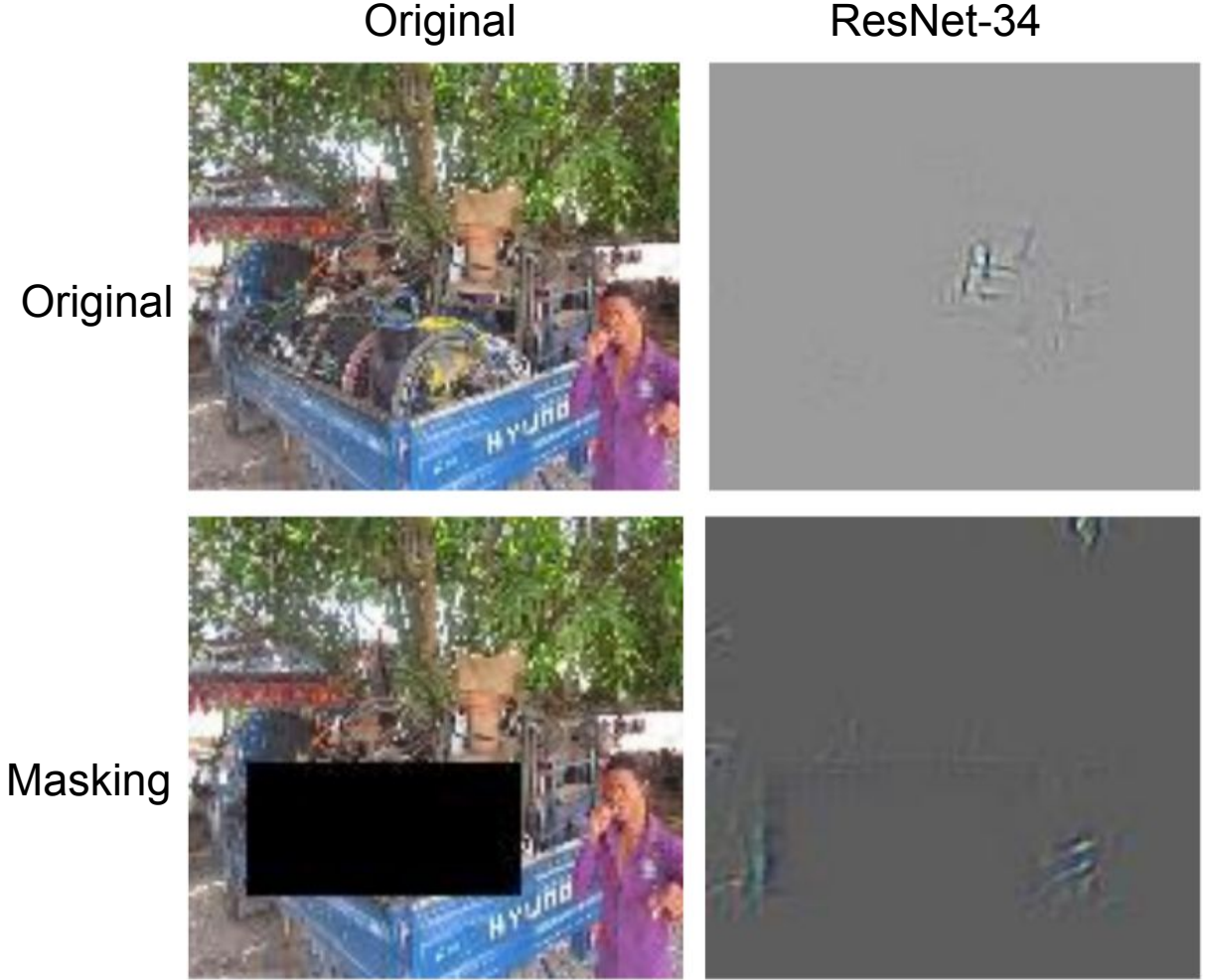


Figure 12: We conduct activation saliency experiment on the COCO-CP trained by bike patterns under partial masking intervention. The guided GradCAM results show current DNNs methods often overfit on the texture and background patterns instead of desired training label(s), which echoes to previous studies [Prakash et al., 2018, Yang et al., 2019, Ilyas et al., 2019].

Given a proxy X , outcome y , binary treatment t and confounder Z , we use the back-door criteria to get:

$$P(y|X, do(t = 1)) = \int_{\mathbf{Z}} P(y|X, do(t = 1), Z)P(Z|X, do(t = 1))dZ \quad (18)$$

Using the intervention manipulation rules, we obtain:

$$P(y|X, do(t = 1)) = \int_{\mathbf{Z}} P(y|X, t = 1, Z)P(Z|X)dZ. \quad (19)$$

The refuting test for all conditional visual model show sustainable performance to the original ATE by random common cause variable test (T_c) and random subset test (T_s) and an ideally nearby zero ATE results on replacing treatment (T_r) with a random variable test. Above validation show our CGM and its associated neural are robust and validated for causal modeling and measurement.

F Evidence Lower Bound of VAE

To validate an Evidence Lower Bound (ELBO) of our CAN, we assume $p(\mathbf{X}, \mathbf{Z})$, where \mathbf{X} is the observed data and \mathbf{Z} is the latent representation. $p(\mathbf{X}, \mathbf{Z})$ can be decomposed into the likelihood and the prior as: $p(\mathbf{X}, \mathbf{Z}) = p(\mathbf{X}|\mathbf{Z})p(\mathbf{Z})$.

Table 15: Validation of causal effect by three causal refuting tests. The causal effect estimate is tested by random common cause variable test (T_c), replacing treatment with a random (placebo) variable (T_r – lower is better), and removing a random subset of data (T_s). TIT outperforms in most tests.

Noise : do(t)	Measurement of ATE			
Method	Original	w/ T_c	w/ T_r	w/ T_s
TIT	0.2432	0.2431	0.0114	0.2481
CEVAE'	0.2414	0.2414	0.0248	0.2329
CVAE'	0.1792	0.1763	0.0120	0.1751

Using Baye’s inference to calculate the posterior gives:

$$p(Z|X) = \frac{p(X|Z)p(Z)}{\int_z p(X|z)p(z)} \quad (20)$$

VAE approximates it with the family of distributions $q_\lambda(Z|X)$, where λ is the variational of parameters for the given family. We minimize the KL divergence to ensure that the approximate distribution used is close to the true posterior:

$$KL(q_\lambda(Z|X)||p(X|Z)) = \mathbb{E}_q[\log(q_\lambda(Z|X))] - \mathbb{E}_q[\log p(X, Z)] + \log p(X). \quad (21)$$

The posterior for inference network will be :

$$q_\lambda^*(Z|X) = \arg \min_{\lambda} KL(q_\lambda(Z|X)||p(X|Z)). \quad (22)$$

However, due to the occurrence of $\mathbf{p}(\mathbf{X})$, the KL is still intractable. We can manipulate the above equation by defining the ELBO:

$$\begin{aligned} ELBO(\lambda) &= \log(p(X)) - KL(q_\lambda(Z|X)||p(X|Z)) \\ &= \mathbb{E}_q[\log p(X|Z)] - KL(\log q_\lambda(Z|X)||p(Z)). \end{aligned} \quad (23)$$

Then, the negative of the ELBO is the loss function used for the neural networks:

$$\begin{aligned} l(\theta, \phi) &= -\mathbb{E}_{q_\theta(z|x)}[\log p_\phi(X|Z)] \\ &\quad + KL(\log q_\theta(Z|X, \lambda)||p(Z)). \end{aligned} \quad (24)$$

θ and ϕ , are the weights and biases of the DNN which are chosen to maximize the ELBO using gradient descent algorithm.

Training Objective of Treatment Inference Transformer. In the TIT setting, where the architecture is adapted from TARnet [Shalit et al., 2017]’s inference network, i.e., split input for each treatment group in t after a shared representation, the objective function \mathcal{L} is given by:

$$\begin{aligned} \mathcal{L} &= \sum_{i=1}^N \mathbb{E}_{q(\mathbf{z}_i|\mathbf{x}_i, t_i, y_i)} [\log p(\mathbf{x}_i, t_i|\mathbf{z}_i) + \log p(y_i|t_i, \mathbf{z}_i)] \\ &\quad + \sum_{i=1}^N \mathbb{E}_{q(\mathbf{z}_i|\mathbf{x}_i, t_i, y_i)} [\log p(\mathbf{z}_i) - \log q(\mathbf{z}_i|\mathbf{x}_i, t_i, y_i)] \end{aligned} \quad (25)$$

For predicting new subject predictions, the treatment assignment t along with outcome y are required. We have introduced Bernoulli distributions which help predict y and t (a binary index of treatment) for new samples with the theoretical foundation from CEVAE [Louizos et al., 2017]. We then leverage bilinear fusion for $q(z|x, y, t, a)$ instead of concatenation [Louizos et al., 2017] and remove Bernoulli sampling for classification label inference. The attention decoding $p(a|x, q(y)) = q(a)$ is incorporating with the known treatment for training.

G Future Work

Discovering Visual Causality beyond Vision Classification Tasks.

In conclusion, we find out causal effect do exist in different DNN-based visual modification methods, and this effect could be visualized to see its effectiveness on understanding targeted DNN layer. By introducing a new extended dataset, COCO-CPs, our CAN networks show competitive visualization results and potential combined with existing saliency-based methods. For future work, we plan to extend our proposed CAN framework to discover visual causality over more visual tasks, such a video detection, cross-model adaption, and obvious question answering (VQA).